

A Numerical Study of Hurricane Erin (2001). Part I: Model Verification and Storm Evolution

Liquang Wu[#], Scott A. Braun^{*}, J. Halverson[%], and G. Heymsfield^{*}

[#]Goddard Earth Science and Technology Center, NASA/Goddard Space Flight Center
Greenbelt, MD

^{*}Laboratory for Atmospheres, NASA/Goddard Space Flight Center, Greenbelt, MD

[%]Joint Center for Earth Systems Technology, University of Maryland, Baltimore County,
Baltimore, MD

submitted to

Journal of the Atmospheric Sciences

October 25, 2003

Corresponding Author: Dr. Liguang Wu, Mesoscale Atmospheric Processes Branch,
NASA/GSFC, Code 912, Greenbelt, MD 20771. liguang@agnes.gsfc.nasa.gov.

Abstract

The Pennsylvania State University-National Center for Atmospheric Research mesoscale model MM5 is used to simulate Hurricane Erin (2001) at high resolution (4-km spacing) from its early development as a tropical depression on 7 September 2001, through a period of rapid intensification into a strong hurricane (8-9 September), and finally into a stage during which it maintains its intensity on 10 September. These three stages of development, intensification, and maintenance in the simulation are in good agreement with the observed evolution of Erin. The simulation shows that during the development and early portions of the intensification stages, intensification is favored because the environmental wind shear is weak and the system moves over a warm tongue of water. As Erin intensifies, the wind shear gradually increases with the approach of an upper-level trough and strengthening of a low-level high pressure system. By 10 September, the wind shear peaks and begins to decrease, the storm moves over slightly cooler waters, and the intensification ends. Important structural changes occur at this time as the outer precipitation shift from the northeastern and eastern sides to the western side of the eye and precipitation begins to surround the entire eye to initiate the development of a secondary wind maximum and an outer eyewall.

The simulation is used to investigate the role of vertical wind shear in the changes of the precipitation structure that took place between 9-10 September by examining the effects of both storm-relative flow changes and changes in the shear-induced tilt. Qualitative agreement is found between the divergence pattern and advection of vorticity by the relative flow with convergence (divergence) generally associated with asymmetric inflow (outflow) in the eyewall region. The shift in the outer precipitation is consistent with a shift in the low-level relative inflow from the

northeastern to the northwestern side of the storm. The changes in the relative flow are associated with changes in the winds as the hurricane moves relative to the upper trough and the low-level high pressure system. Examination of the shear-induced tilt of the vortex shows that the change in the tilt direction is greater than that of the shear direction as the tilt shifts from a northerly orientation to northwesterly. Consistent with theory for adiabatic vortices, the maximum low-level convergence and upper-level divergence (and the maximum upward motion) occurs in the direction of tilt. Consequently, both mechanisms may play roles in the changes in the precipitation pattern.

1. Introduction

Tropical cyclones are very complex atmospheric systems in terms of their interacting physical processes on multiple scales. Studies to date have gained considerable insights into the mechanisms of their formation and development, especially through various simplified numerical models (e.g., Ooyama 1969, Emanuel 1989, Montgomery and Enagonio 1998). Compared to improvements in hurricane track forecasts, the skill level in prediction of tropical cyclone structure and intensity remains relatively low. One reason is that the physical mechanisms related to intensity change are not well understood (Neuman 1997). Recent studies have suggested that hurricane intensity change is closely associated with interactions with the large-scale environment [e.g., shear (Jones 1995; Frank and Ritchie 1999, 2001; Black et al. 2002)], variations in and feedbacks to the sea-surface temperature (Shay et al. 2002, Chan et al. 2002), and with processes associated with inner-core convection and vortex dynamics (Montgomery and Kallenbach 1997, Schubert et al. 1999), particularly the eyewall cloud region.

For this reason, increasing attention has been given to sophisticated numerical models that can explicitly resolve multi-scale atmospheric processes within tropical cyclones. The Pennsylvania State University-National Center for Atmospheric Research fifth-generation, nonhydrostatic mesoscale model (MM5, Dudhia 1993, Grell et al. 1995) has been used frequently to study tropical cyclones. For example, Liu et al. (1997, 1999) simulated Hurricane Andrew (1992) and described both its inner-core structure and its intensification. Braun and Tao (2000) investigated the sensitivity of high-resolution (4 km) simulations of Hurricane Bob (1991) to planetary boundary layer parameterizations, while Braun (2002) examined the structure of the eyewall and issues related to buoyancy in eyewall updrafts using a horizontal grid spacing of 1.3 km. Davis and Bosart (2001, 2002) studied the transformation of a weak baroclinic disturbance

into Hurricane Diana (1984). Frank and Ritchie (1999, 2001) investigated the structure and intensity changes caused by vertical wind shear in idealized simulations. Chen and Yau (2001) studied inner-core spiral potential vorticity (PV) bands and found that the propagation properties of the PV bands were consistent with predictions of vortex Rossby wave theory. As demonstrated by these studies, the MM5 system is highly capable of simulating the evolution and structure of tropical cyclones, with either idealized or realistic initial conditions. Our motivation for the present study is to explore further the nature of hurricane development and intensity change by simulating Hurricane Erin (2001), which occurred during the field phase of the National Aeronautics and Space Administration Fourth Convection and Moisture Experiment (CAMEX-4).

A major part of the intensity change problem is the interaction of a tropical cyclone with external influences including large-scale environmental flows and the underlying ocean characteristics. The roles of environmental flows have been investigated in terms of the resulting eddy fluxes (Molinari and Vollaro 1989, 1990), the associated divergence (Bosart et al. 2000), the superposition of potential vorticity anomalies (Molinari et al. 1995, 1998), and the environmental vertical wind shear (Jones 1995; Frank and Ritchie 1999, 2001). The negative impact of vertical shear on hurricane intensity is well established, whereas the other environmental effects remain open for debate.

Since intensity change is ultimately related to inner-core processes in a tropical cyclone, even when externally forced, a critical issue is how the inner-core dynamics respond to large-scale environmental influences. Recent studies, both observational and numerical, have shown that in response to vertical wind shear the structure of the eyewall region becomes significantly asymmetric with a dominant azimuthal wavenumber-1 component (e.g., Jones 1995; Bender

1997; Reasor et al. 2000; Frank and Ritchie 1999, 2001; Black et al. 2002). Several mechanisms have been proposed by which vertical wind shear produces asymmetries in vertical motions in adiabatic vortices. These include 1) the balanced response to a tilted vortex producing upward motion in the downtilt direction (Raymond 1992, Jones 1995, Wang and Holland 1996, Frank and Ritchie 1999) and 2) interaction of the vortex flow with temperature anomalies generated by the vortex tilt, which produces upward motion 90° to the right of the tilt direction (Jones 1995). Diabatic vortices tend to have much smaller tilts than their adiabatic counterparts possibly as a result of stronger vertical coupling of the lower and upper vortices by the diabatic heating effects (Wang and Li 1992, Flatau et al. 1994). Reasor et al. (2003) have argued that the moist dynamics associated with diabatic vortices are not fundamentally different than the adiabatic vortex dynamics. They show that, if the shear is not too strong, adiabatic vortices are quite resilient to shear since the adiabatic dynamics tend to suppress departures from an upright state. The tilt asymmetries are dissipated through two types of vortex Rossby waves: sheared vortex Rossby waves and a discrete, quasi-mode. Reasor et al. (2003) suggest that moist processes simply enhance the adiabatic dynamics.

In this study, we examine the evolution of Hurricane Erin and its response to increasing vertical wind shear. Section 2 gives a brief overview of Hurricane Erin and describes the model setup. Section 3 provides an in-depth validation against available observations of the intensity and storm structure. Section 4 describes the development of Erin through three stages of the evolution including formation, intensification, and maintenance and relates structural changes during the evolution from the intensification to the maintenance stages to the evolution of the vertical shear near the storm. Conclusions are provided in section 5.

2. Simulation description

a. Overview of Hurricane Erin (2001)

As with many Atlantic tropical cyclones, Hurricane Erin can be traced back to a tropical wave that emerged from western Africa on 30 August. The system strengthened into Tropical Storm Erin by 0600 UTC 2 September as the central pressure fell to 1002 mb. However, southwesterly vertical wind shear associated with an upper-level trough to the northwest prevented Erin from intensifying further (Zehr 2002). On 5 September, its development was further disrupted, and the system became an area of disturbed weather. The minimum surface pressure was as high as 1015 mb.

About a day later, the vertical shear weakened and a surface circulation redeveloped in the northern part of the area of disturbed weather that was associated with Erin (Fig. 1a). It moved north-northeastward, then north-northwestward, and regained tropical storm intensity at 1800 UTC 7 September with a central pressure of 1007 mb (Fig. 2). Erin continued to strengthen and became a hurricane by 0000 UTC 9 September, reaching its peak intensity near 0000 UTC 10 September. Interestingly, despite increasing vertical wind shear on 9 September, Erin continued to intensify throughout the day. By 0000 UTC 10 September, the vertical wind shear peaked and Erin began moving over cooler waters (Fig. 1b). In response, Erin's intensification ended (Fig. 2) and it maintained its peak intensity for about 18 h before beginning to weaken. By 0000 UTC 15 September, Erin had weakened into a tropical storm and eventually transitioned into an extratropical system.

The model integration begins at 0000 UTC 7 September when Erin was an area of disturbed weather. Erin was identifiable in the analysis as a weak tropical depression (Fig. 1a, $\sim 60^\circ$ W, 22° N) with a central pressure of 1013 mb and a maximum wind of about 15 m s^{-1} (Fig.

2). The sea-surface temperature (SST) field (Fig. 1b) indicates that the tropical disturbance was situated over a broad area of warm ocean waters exceeding 301 K. The simulation was terminated at 0000 UTC 11 September, shortly after Erin had begun to weaken. The 96-h integration covers several important periods in the life cycle of Hurricane Erin including its formation, intensification, and maintenance stages.

b. Simulation description

The 96-h simulation of Hurricane Erin is conducted using the nonhydrostatic version of MM5 (V3.4). Three two-way interactive domains on Mercator map projections are used with grid spacings of 36, 12, and 4 km and with domain sizes of 145×175, 196×175, and 151×151 grid points, respectively. The coarsest grid is centered at 31.0° N, 73.0° W. There are 28 uneven σ levels with higher resolution in the planetary boundary layer (PBL). The top of the model is set to 50 mb. A time step of 90 s is used on the coarsest grid and is reduced by a factor of three for each successive nest.

The MM5 system provides various options for model physics such as cumulus convection, planetary boundary layer, cloud microphysics, and radiation. Choices of model physics are often critical to the successful simulation of tropical cyclones (Liu et al. 1997; Braun and Tao 2000; Davis and Bosart 2002). Because of the larger grid spacings in domains 1 and 2, cumulus parameterization is necessary for these grids. Tests of the various cumulus parameterization schemes for this case indicate that a hurricane is only obtainable when using the Betts-Miller cumulus parameterization scheme, which is also used by Liu et al. (1997), Braun and Tao (2000), and Davis and Bosart (2002). Other model physics options include the Goddard Cumulus Ensemble model cloud microphysics; a modified version of the Blackadar PBL parameterization, in which the surface roughness calculations for momentum, temperature, and

moisture follow Garratt (1992) and Pagowski and Moore (2001); and the cloud radiative scheme of Dudhia (1989).

The initial and boundary conditions for the 36-km domain are obtained from 12-hourly National Centers for Environmental Prediction (NCEP) surface and upper-air global reanalysis data sets. The SST data are derived from the NCEP SST analysis. The analysis fields, including temperature, geopotential height, winds, and dewpoint at mandatory pressure levels and with horizontal resolution of $2.5^{\circ}\times 2.5^{\circ}$ are interpolated horizontally to model grid points and vertically to the model σ levels. No special observations are available near the initial time and no bogus vortex is included. The initial conditions for the nested domains are obtained by interpolating fields from their respective mother domains.

The simulation is initialized at 0000 UTC 7 September. Additional simulations initialized at other times show that this initialization time provides the best representation of Erin's evolution. During the first 12 h, only the outer-most domain is active. The 12-km and 4-km domains are activated at 1200 UTC 7 September (12 h) and 0000 UTC 8 September (24 h), respectively.

3. Simulation validation

Comparisons of the maximum surface wind speed and minimum sea-level pressure between the simulation and best-track data are shown in Fig. 2. The simulated deepening is nearly identical to the observations until 66 h (1800 UTC 9 September). Thereafter, the simulated storm's central pressure continues to deepen while the observed pressure remains nearly steady or rises slightly. Central pressure and maximum wind speed have generally been used interchangeably to represent hurricane intensity. Figure 2 indicates that the relationship between minimum pressure and maximum wind speed can be complex as the simulated

maximum wind levels off or decreases slightly after 66 h while the minimum pressure continues to decrease. Schubert et al. (1999), Kossin and Schubert (2001), and Braun et al. (2003) have suggested that this result can occur following the axisymmetrization process. Specifically, the inward mixing of eyewall vorticity weakens the tangential winds of the eyewall, increases winds in the eye, and lowers the central pressure.

The simulated storm intensifies somewhat more rapidly than observed. The simulated storm reaches tropical storm strength as early as 6 h (0600 UTC 7 September, 12 h before observed) and reaches hurricane intensity by 40 h (1500 UTC 8 September, 5 h before observed). The earlier intensification occurs partly because of an abrupt increase in the maximum winds after 12 h that arises from initiation and spin-up of fields on the 12-km grid. The subsequent simulated development agrees well with the observations. After 66 h, the maximum winds of the simulated and observed hurricanes are quasi-steady, with the observed winds being a little stronger.

Figure 3 shows comparisons of Erin's observed track with that simulated. In the simulation, the tropical depression forms to the southwest of the observed location. The displacement of the simulated track from that observed may result from uncertainty in the location of the incipient cyclone within the large-scale low pressure area. Gray (1998) suggests that the location of an incipient cyclone within a larger low pressure region may be closely associated with a strong inward flux of eddy angular momentum, which can trigger new outbreaks of deep cumulus convection. Gray's results suggest that in order to predict the initial location of the incipient cyclone, a precise description of the inward momentum flux in the initial fields is required. However, the $2.5^{\circ} \times 2.5^{\circ}$ resolution of the NCEP analysis is not adequate for this purpose. Another discrepancy in the track prediction is that the simulated storm takes a more

northwestward track than that observed during the last 24 hours (during 10 September). This discrepancy likely results from errors in the simulation of the large-scale circulation. Despite these discrepancies, the track of the simulated storm agrees reasonably well with observations, especially considering that no bogus vortex is included in the initial conditions and that the storm develops from a broad region of low pressure.

Validation of the storm structure is performed using observed surface wind fields (courtesy of Mark Powell, National Oceanographic and Atmospheric Administration/Hurricane Research Division), rainfall rates derived from the Tropical Rainfall Measuring Mission (TRMM) satellite, and special observations from NASA aircraft during CAMEX-4. Two surface (10 m) wind analyses are available for Erin, valid at 1930 UTC 9 September and 1800 UTC 10 September, respectively (Figs. 4 and 5). For comparison, the simulated wind fields at the lowest model level (38 m) for 2000 UTC 9 September and 1800 UTC 10 September are also shown in these figures. Figure 4a indicates that the analyzed surface winds are fairly symmetric with local wind maxima on the northwestern, eastern, and southern sides of the eyewall with the largest value of 52 m s^{-1} to the east. The simulated maximum winds are more asymmetric with local maxima on the northwestern and northeastern sides of the eyewall and weaker winds to the south. The strongest winds in the analysis are concentrated near the eyewall, while in the simulation strong winds are spread out over a larger area. The simulated maximum is 46 m s^{-1} , about 6 m s^{-1} weaker than the analysis. At 1800 UTC 10 September (Fig. 5a), the surface analysis shows a more asymmetric wind field with maximum winds exceeding 40 m s^{-1} on the northern side, about 5 m s^{-1} weaker than the best track data. The simulated winds show the same general asymmetry and the wind maximum of 46 m s^{-1} is in good agreement with the best track data.

Erin was viewed by the TRMM Microwave Imager (TMI) on several occasions on 9-10 September. The distribution of precipitation retrieved from the TMI is used for validation since the narrow swath of the TRMM radar provides inadequate sampling. The TMI data provide sufficient information on the general structure of Erin in the core region and its changes from 9-10 September. Figures 6 and 7 show the retrieved precipitation rates at 1011, 1326, and 1504 UTC 9 September and at 1142, 1315, and 1447 UTC 10 September, respectively. The horizontal resolution of the TMI is about 10 km, so smaller-scale convective cells are not well resolved. The simulated radar reflectivity fields are displayed for comparison. Our purpose here is simply to compare the qualitative features of the precipitation structure indicating the degree and evolution of asymmetries in both the eyewall and outer rainbands. In terms of the locations of the outer and inner rainbands relative to the storm center, the simulation agrees well with the observations. Earlier on 9 September, the TMI data show maximum precipitation generally on the northwest side of the eyewall (Fig. 6), with an increasing trend toward axisymmetry at later times (Figs. 6b, 6c), consistent with the wind analysis (Fig. 4a). Outer precipitation bands occur in the northeastern quadrant, approximately in the downshear to downshear-right direction similar to the observations of Corbosiero and Molinari (2003), who found a downshear-right preference for lightning in the outer bands of hurricanes in moderate-to-strong shear. The eyewall and outer bands are separated by a gap, with a connecting band (Willoughby et al. 1984) on the northern side of the eyewall. The simulated precipitation structure is very similar, albeit with somewhat greater asymmetry in the eyewall and considerably less distinction between the eyewall and outer rainbands. The broader distribution of precipitation on the northern side of the eyewall is likely indicative of a connecting band. Maximum eyewall precipitation occurs on the northwestern, or downshear-left, side and outer convective bands are generally found on the

northern side and around to the eastern side. By 10 September (Fig. 7), in both the TMI data and the model, the eyewall is asymmetric with maximum precipitation on the western to northwestern sides, while the outer convection shifts to the western side of the storm and convection begins to surround much of the eyewall. These results clearly suggest that while the detailed structure may vary between the TMI data and model, the evolution of the general precipitation structure is captured quite well in the simulation.

The ER-2 Doppler radar (EDOP) is an X-band (9.6 GHz) radar with dual 3° beamwidth antennas fixed at nadir and 30° forward of nadir. EDOP, described in detail by Heymsfield et al. (1996), provides high-resolution vertical profiles of radar reflectivity and Doppler velocity. Calculation of vertical air motion from the Doppler velocities has been described by Heymsfield et al. (1999, 2001). Aircraft motions are first removed using flight parameters from the ER-2 inertial navigation system (the nadir antenna is not exactly at nadir, so some correction is necessary). Vertical air motions are then obtained by subtracting hydrometeor fall speeds from the Doppler velocities, where the fall speeds are estimated based upon reflectivity measurements following Marks and Houze (1987) and Black et al. (1996). The resulting vertical motion estimates can be subject to errors of several meters per second in strong convective regions as a result of improper fall speeds, especially below the melting level. Above the melting level, errors should be smaller as a result of the typically smaller fall speeds of ice particles.

Figure 8 shows reflectivities and estimated vertical motions for two passes across the eye of Erin between 1800-2000 UTC 10 September. The first pass from northwest to southeast (Figs. 8a, 8b) shows outward sloping eyewalls and multiple rainbands at larger radius. On the northwestern side, strong low-level upward motion is indicated (although subject to possible error) in the eyewall with weaker upward motions (2-4 m s⁻¹) aloft. Heavy precipitation occurs in

multiple reflectivity cells that comprise a rainband (120-200 km) outward from, but immediately adjacent to the eyewall. Further outward (10-80 km), another rainband with multiple embedded cells occurs, with the inner-most cell possessing fairly strong upward motion ($> 4 \text{ m s}^{-1}$). On the southeastern side, the eyewall contains substantial upward motion throughout the troposphere and an outer rainband (290-350 km) occurs with substantial upward motion in its inner-most cell. The second pass (Figs. 8c, 8d), from west to east, shows a very similar structure, but with little upward motion indicated above the melting level in the eyewall. The lack of updrafts is not surprising given that updrafts typically occupy only a small percentage of the eyewall area (Jorgensen et al. 1985, Braun 2002, Braun et al. 2003) so that any given pass through the eyewall has a relatively small chance of sampling a strong updraft. As in the earlier cross section, the strongest upward motions in the rainbands occur in the inner-most cells.

The simulated vertical structure of Erin is depicted in Fig. 9, which shows vertical cross sections of simulated reflectivity and vertical velocity for two vertical planes oriented approximately in directions similar to the ER-2 passes (see Fig. 9c). The northwest to southeast cross section (Fig. 9a) shows strong eyewall vertical motion ($\sim 4\text{-}5 \text{ m s}^{-1}$) on the northeastern side with an adjacent wide area of stratiform rain with embedded cellular structure. On the southeastern side, the model shows only a shallow precipitation feature associated with the eyewall ($\sim 325 \text{ km}$) compared to the deep convection observed (Fig. 8a). Also, the convection outside the eyewall on this side is generally much shallower than observed. In the west to east cross section (Fig. 9b), the vertical motions are generally weak with the strongest upward motions in one of the rainbands on the eastern side. In this cross section, a deeper reflectivity core is seen on the eastern side of the eyewall, but contains only weak upward motion. The outer-most precipitation cells on the western side are shallower than observed. The simulated

vertical structure suggests that the occurrence of stronger upward motion in the eyewall in the northwest to southeast cross section and the weaker vertical motion in the west to east cross section are generally similar to those observed. However, a key difference is seen in the depth of the reflectivity cells in the rainbands, particularly on the eastern side of the storm. It is unclear whether this discrepancy results from suppression of the vertical motions by the large-scale or vortex-scale flow, from deficiencies in the model physics, or from the relatively coarse 4-km grid spacing that only crudely resolves the cloud and precipitation features.

During 1600-2030 UTC 10 September, 19 dropsondes were released from the NASA DC-8 and ER-2 aircraft. Halverson et al. (2003) used these dropsonde profiles to construct a cross section of Erin's warm-core structure. They created a reference environmental temperature profile containing data from a DC-8 dropsonde below 329 mb at 1800 UTC in the clear air 610 km southeast of Erin's center and from an ER-2 dropsonde above 329 mb located 340 km to the northeast of the center. This same environmental profile is used here to create a cross section of the warm core from the simulation.

Figure 10a shows the observed warm-core temperature anomaly from Halverson et al. (2003), while Fig. 10b shows the model anomaly field superimposed on the simulated radar reflectivity. The observed temperature anomaly depicts a maximum value just over 11 K between 400-500 mb. The temperature anomaly tends to spread out laterally at upper levels compared to lower levels. Negative temperature anomalies occur at low levels outside of the inner core. The simulated temperature anomaly is remarkably similar in many respects. Peak values of just over 11 K are found between 400-500 mb, the warm anomaly spreads out laterally at upper levels, and weak negative anomalies are found at low levels outside the eyewall. One key difference is that in the simulation, the warm anomaly is confined largely within the eye with

strong horizontal temperature gradients in the eyewall. In the analysis, insufficient data was available to observe the strong radial gradients so that the contours are spread out more evenly between dropsondes locations. Another key difference is in the structure of the anomalies at upper levels above 300 mb. The observed anomaly extends upward to just over 200 mb before encountering the tropopause. In the simulation, the anomaly weakens above 300 mb and the strong vertical gradient is absent. This difference may be related to the relatively coarse vertical resolution in the model above 300 mb where the grid spacing is between 700-1000 m.

4. The simulated evolution of Erin

In the following analysis, the circulation of Erin is decomposed into its azimuthally symmetric and asymmetric components. Since the symmetric circulation is usually one order of magnitude stronger than the asymmetric circulation, a slight shift of the storm center location can lead to significant differences in the asymmetric circulation, especially in the inner region. For example, in the hurricane inner-core region, eyewall mesovortices can occur (Schubert et al. 1999, Kossin and Schubert 2001, Braun et al. 2003) and can be associated with the minimum pressure (Marks and Black 1990; Black and Marks 1991). In such cases, the center defined by the location of the minimum central pressure (the pressure center) or the minimum wind (the circulation center) may not adequately represent the geometric center of the hurricane. In a study of Hurricane Bob (1991), Braun (2002) derived an estimate of the hurricane's geometric center by minimizing the azimuthal variance of the pressure field at all radii between the center and the outer portion of the eyewall. In the present study, the hurricane center is defined as that which maximizes the symmetric tangential wind. This definition minimizes aliasing of the symmetric wind component onto the asymmetric component. In order to determine the hurricane center, a variational approach is used to adjust the location of the center until the maximum azimuthal

mean tangential wind speed is obtained. Calculations show that the hurricane center locations defined in this way are very close to those determined by the method of Braun (2002). Center locations are determined only after 24 h when the system is of tropical storm intensity.

Figure 11 shows Erin's evolution in terms of the azimuthal mean tangential wind and simulated radar reflectivity at the lowest model level (38 m) while Fig. 12a depicts the evolution of the eyewall's vertical structure in terms of the azimuthally and radially (over the eyewall region) averaged vertical and radial winds. Since the eyewall updrafts are generally located slightly inward of the eyewall radial inflow and outflow, the vertical motions are averaged over a radial band slightly inward of that for radial velocity. As suggested in Figs. 2 and 11, the intensity of Erin evolves through three distinct stages. In the first stage, called the formation stage, slow intensification of the initially broad symmetric circulation occurs in association with a weak symmetric component of convection as the central pressure falls about 16 mb and the mean tangential winds increase to 20 m s^{-1} prior to 36 h. During this time, the radius of maximum wind (RMW) quickly decreases from 125 to 70 km. The contraction of the eyewall implies a significant increase in the maximum vorticity and a rapid enhancement of the secondary circulation (Fig. 12a). In addition to inflow in the boundary layer, significant midlevel inflow occurs during this formation stage, which agrees with the composite study by Lee (1989).

During the second stage (36-72 h, hereafter called the intensification stage), the eyewall continues to contract, the symmetric reflectivities increase, and the storm intensifies rapidly (Figs. 2 and 11). Erin's size, as indicated by the 20 m s^{-1} isotach in Fig. 11, expands with time. As shown in Fig. 12a, outflow occurs at middle and upper levels while inflow is primarily at lower levels. Upward motion is at its strongest and deepest during this phase with its maximum at middle levels.

In the third stage (after 72 h, referred to as the maintenance stage), the eyewall contracts slowly and there is little intensification in the symmetric tangential winds. The reflectivity in the eyewall region (Fig. 11) significantly decreases during this stage while the convection outside the primary eyewall at first decreases (78-84 h) and then redevelops after 84 h as convection begins to surround the eyewall (Fig. 7). Much weaker mean upward motion corresponds with the decreased reflectivities in the eyewall (Fig. 12a). As in the formation phase, significant mid-level inflow occurs. By 96 h, in response to the enhanced convection between 80-100 km, a secondary wind maximum develops (Fig. 13) in the azimuthal mean flow. The secondary circulation at this time shows relatively weak ascent in the eyewall and stronger ascent and outflow near the secondary wind maximum.

In summary, as indicated in Figs. 2, 11, and 12a, Erin evolved through three stages of development (formation, intensification, and maintenance) and its structure changed dramatically from one stage to another. Here, we focus mainly on the changes in the structure and intensity during the transition from the intensification to the maintenance stages, how these changes are related to the evolution of the large-scale shear, and how the shear evolution is governed by the location of the storm within the larger-scale synoptic pattern. The structural changes associated with the transition from the formation phase to the intensification phase will be reserved for future study.

First, we briefly discuss factors aiding the rapid intensification of Erin. It is known that tropical cyclone maximum potential intensity is related to the temperature of the underlying ocean (Emanuel 1988, Holland 1997). Shay et al. (2000) suggested that the rapid intensification of Hurricane Opal (1995) was associated with a warm pool or warm-core eddy. Using the MM4 model coupled with a simple mixed-layer ocean model, Chan et al. (2002) confirmed this

intensification effect. Emanuel (1988) derived a relationship between the central pressure of a storm at its maximum potential intensity and the sea-surface temperature by assuming that the air rises along slanting moist-neutral angular momentum surfaces extending outward in the outflow layer. Following this model, the minimum attainable central pressure decreases with increasing SST (assuming fixed outflow temperature). As shown in Fig. 1b, Erin passes over a warm pool of 302 K water between 36-60 h. Since crossing of the warm pool coincides with the rapid deepening of Erin, the intensification is at least partially the result of the elevated SST. After 60 h, Erin moves northward of this warmer water and the decrease in SST may be contributing to the weakening of Erin's circulation (Halverson et al. 2003). However, as will be shown below, changes in the environmental wind shear are also an important factor in Erin's intensity changes.

The evolution of the large-scale mean flow is estimated by a time series of the vertical profile of the area-mean winds averaged over a circle of 300-km radius centered on the storm (Fig. 12b). During the formation stage, both the mean wind and its vertical shear are generally weak. As shown in Fig. 14a, Erin is located near the center of a col at 200 mb and just south of the ridge axis that extended from east to west. At 850 mb (Fig 14b), the storm is west of the subtropical high. As a result, Erin experiences weak southerly to southeasterly flow at all levels and little vertical shear. This weak shear is likely critical to the development and rapid intensification during this stage and the first part of the intensification stage.

Between 42-72 h, the mean winds gradually strengthen. The approach of an upper-level trough from the west (Fig. 14c) increases the southwesterly flow near Erin while at low levels Erin is located just south of a relatively strong high pressure system and is embedded in substantial easterly to southeasterly flow. Consequently, stronger southwesterly shear develops and eventually reaches sufficient strength to halt intensification of the storm. By 84 h (Figs

14e,f), weakening of the upper trough and low-level high leads to a gradual weakening of the mean flow. As Erin moves northward relative to the upper trough center and westward relative to the low-level high, the upper-level flow becomes more southerly while the low-level flow shifts to easterly and eventually northeasterly (Fig. 12b). As a result, during the maintenance stage, the shear weakens and the shear direction shifts from southwesterly to south-southwesterly. As will be shown below, these changes in the shear apparently impact the storm structure. Although the mean flow in Fig. 12b contains both the effects of the environmental flow and the asymmetric flow resulting from beta gyres (caused by advection of planetary vorticity by the vortex), Figs. 12b and 14 suggest that the large-scale environmental flow dominates the mean flow.

Comparison of Figs. 12a and 12b suggests that the onset of the weakening of the eyewall upward motion occurs at about the time of the peak vertical wind shear near 0000 UTC 10 September (72 h). Several changes in the structure of the storm, both observed and simulated, occur during this transition from the intensification to the maintenance stages. The TRMM rainfall data and the simulated reflectivities in Figs. 6 and 7 indicate a shift in the precipitation outside of the eyewall from the northern or northeastern to the western side of the storm and a gradual encircling of the eyewall by a developing outer ring of convection. This pattern is even more evident in the time-averaged reflectivity fields for 9 September and 10 September. On 9 September (Fig. 15a), the area of heaviest precipitation, including the eyewall and the portions of the outer rainbands closest to the eyewall, is located on the northwestern and northern sides of the storm, while more cellular portions of the outer bands (see Fig. 6) lay to the northeast and east on the downshear-right side of the storm (Corbosiero and Molinari 2003). Little outer precipitation occurs on the southern side. On 10 September (Fig. 15b), the area of heaviest precipitation is on the western and northwestern sides of the storm. The more cellular portions of

the outer bands have weakened and do not exhibit a distinct downshear-right preference, consistent with the weakening of the shear. Furthermore, convection has developed on the southern half of the storm so as to encircle the inner core of precipitation. This result, combined with the finding of a weak secondary wind maximum near the radius of the outer precipitation, suggests that a secondary eyewall may be beginning to form. Interestingly, this secondary eyewall begins to form about 12 h after relaxation of the vertical wind shear. In their simulation of Hurricane Bonnie (1998), Zhu et al. (2003) described the formation of a secondary eyewall that occurred approximately 24-36 h after strong large-scale shear weakened. It is unclear what role, if any, this relaxation of the shear plays in the development of this outer ring of convection, but we can speculate on one possible role as follows. When the shear is large, the outer convection is clearly favored on the downshear-right side, consistent with Corbosiero and Molinari (2003). As the shear relaxes, the favoring of convection downshear diminishes and allows for greater likelihood of convection at any location around the storm, thus making it possible for an outer ring to form.

It has been well demonstrated that precipitation, particularly in the eyewall, tends to occur on the downshear-left side (Bender 1997; Frank and Ritchie 1999, 2001; Reasor et al. 2000; Black et al. 2002). As previously mentioned, the pattern in Erin is similar. Overlaid on the reflectivity patterns in Fig. 15 are arrows indicating the direction of the 1-10 km (roughly 850-200 mb) layer shear averaged over the two 24-hour periods. From 9 to 10 September, the average shear direction rotates cyclonically by about 20-30° (depending on the layer chosen for the shear estimate). The precipitation tends to occur on the downshear-left side and this change in the shear direction accounts for a portion of the shift in precipitation, but may not be solely responsible given the relatively small magnitude of the change. While it is correct to say that the

precipitation is downshear-left, it says nothing about why that is the case.

Two mechanisms have been hypothesized about how shear produces the asymmetry. One is related to the storm-relative flow (Bender 1997) while the other is related to the vortex tilt (Raymond 1992, Jones 1995). To investigate the effect of relative flow, the storm-relative asymmetric flow is overlaid in Fig. 15. Bender (1997) argued that the direction of the relative flow controls the location of the precipitation maxima as follows. Assuming a first-order balance in the vorticity equation between horizontal vorticity advection and the stretching or compression of vorticity by divergence, one expects convergence (divergence) where there is inflow (outflow) in the eyewall. On 9 September, relative inflow occurs on the northeastern side of the storm while on 10 September, it shifts to the northern to northwestern side. Figure 16 shows the relative flow at both upper and lower levels superimposed on the asymmetric divergence. Qualitatively, the vorticity balance argument is valid since at lower and upper levels, convergence (divergence) occurs where there is relative inflow (outflow), although the peak divergence at upper levels lies somewhat to the left of the primary outflow. Changes in the relative flow can occur as a result of changes in the shear or in storm motion. In the simulation, a distinct change in the storm motion occurs (Fig. 3) near 0000 UTC 10 September as the motion changes to a more northwesterly direction. However, the shift in the outer precipitation occurs in both the observations and the simulation while the change in storm motion occurs only in the simulation. This result suggests, then, that the important changes in the relative flow arise because of changes in the environmental winds.

Wavenumber 1 asymmetries in vertical motion can also arise as a result of vortex tilt. In tilted adiabatic vortices, balance constraints require that a cold (warm) temperature anomaly occur in the downtilt (uptilt) directions (Raymond 1992, Jones 1995). These temperature

anomalies are created by upward (downward) air motion on the downtilt (uptilt) sides of the vortex. Jones (1995) shows that, subsequently, the vortex flow interacts with these temperature anomalies to produce upward motion 90° to the right of the tilt direction. However, simulations of diabatic vortices (Frank and Ritchie 1999, 2001) have suggested that diabatic heating generally destroys the cold anomaly. Frank and Ritchie (2001) argue that since their simulated diabatic vortices exhibit little tilt, the mechanism of Bender (1997) likely accounts for the simulated asymmetries. However, even a small amount of tilt may be capable of producing asymmetries (Reasor et al. 2000, Braun et al. 2003). Reasor et al. (2003) argue that the moist dynamics associated with diabatic vortices are not fundamentally different than the adiabatic dynamics. First, they show that, as long as the shear is not too strong, adiabatic vortices are quite resilient to shear. They examine the tilting of a vortex by shear and find that a damping mechanism intrinsic to the dry adiabatic dynamics suppresses departures from an upright state. This realignment occurs through projection of the tilt asymmetry onto two types of vortex Rossby waves: a quasi-mode, or discrete, vortex Rossby wave that causes long-lived precession of the upper part of a tilted vortex relative to the lower part, and sheared vortex Rossby waves in which the radial shear of the swirling flow axisymmetrizes tilt asymmetries, resulting in short-lived precession and more rapid reduction of the tilt. In the case of a weakly damped quasi-mode, the vortex approaches a steady state in which it tilts approximately 90° to the left of the shear vector. Reasor et al. (2003) suggest that the effects of moisture simply enhance this process.

To examine the impact of vortex tilt, the center of the vortex at 8 km is calculated every hour during 9-10 September. The tilt of the upper vortex relative to its surface location is superimposed on the divergence field in Fig. 16 while the temporal and azimuthal variations of the tilt are overlaid on the radially averaged (16-100 km) vertical motion and potential

temperature at 5 km in Fig. 17. From Fig. 16, it can be seen that the maximum low-level convergence and upper-level divergence occurs exactly in the downtilt direction. On 9 September, the average tilt is approximately 20 km and directed to the north, roughly 60° to the left of the shear vector, while on 10 September, the tilt decreases slightly to 18 km and rotates cyclonically so that it is directed 90° to the left of the shear. In Fig. 17, the mean eyewall upward motion is nearly aligned or slightly to the right of the direction of vortex tilt. A slight bias to the right may arise since the outer convection generally occurs downtilt or downtilt-right while the eyewall convection is generally in the downtilt direction. A cold anomaly in the potential temperature field is collocated with the upward motion. The direction of the peak upward motion and minimum temperature generally follows the direction of tilt, changing from the northeast side on 9 September to the northwest side on 10 September. The alignment of the upward motion, cold temperature anomaly, and vortex tilt suggests that the vortex is nearly balanced and that the change in the tilt of the vortex is primarily responsible for the shift in the precipitation pattern between 9 and 10 September. Clearly, the cyclonic rotation of the shear vector during this period accounts for part of the change in vortex tilt. However, the change in tilt direction is larger than that of the shear direction. It is possible that the stronger shear on 9 September causes the tilt to be somewhat more aligned with the shear and that weakening of the shear on 10 September allows the tilt to approach 90° relative to the shear direction, which Reasor et al. (2003) claim is the steady-state tilt direction for a weakly damped quasi-mode.

The collocation of the upward motion and cold anomaly differs from the expectations of the behavior of adiabatic vortices. Jones (1995) and Wang and Holland (1996) find that for adiabatic vortices, the upward motion tends to occur 90° to the right of the cold anomaly. Frank and Ritchie (1999), using idealized simulations at 15-km horizontal resolution, show that during

early stages after shear is imposed the precipitation is dominated by the convective parameterization and the maximum upward motion is located downshear-right, consistent with Jones (1995) and Wang and Holland (1996). However, once grid points in the eyewall reach saturation and the precipitation is dominated by the explicit microphysical parameterization, the maximum upward motion shifts to the downshear-left side. They suggest that grid-scale latent heating eliminates the downtilt temperature anomaly so that upward motion occurs in the downshear to downshear-left direction. In a simulation of Hurricane Bonnie (1998), Braun et al. (2003) find that the cold temperature anomaly aligns with the eyewall upward motion and vortex tilt. They provide two explanations for why the cold anomaly occurs despite latent heating. First, thermodynamic budgets derived from a simulation of Hurricane Andrew (1992) by Zhang et al. (2002) suggest that adiabatic cooling in eyewall updrafts may slightly exceed the latent heating so that net cooling occurs in the eyewall. Second, even if the latent heating exactly balances the adiabatic cooling, a cold anomaly can arise through strong adiabatic warming in dry, subsiding air on the uptilt side. Braun et al. (2003) argue that independent of how the cold anomaly forms, it appears that the interaction of the mean vortex flow with the temperature anomaly field produces weaker forcing for vertical motion than the more direct effects of the tilt. For example, assuming that the magnitude of the temperature anomaly field is strongest at middle levels, the mean vortex flow moving through this anomaly field produces vertical motion that peaks at those levels. Since this vertical motion is relatively far removed from the boundary layer, convection is less likely to occur. In contrast, if the tilting of the vortex produces low-level convergence and upper-level divergence in the downtilt direction, then deep convection with roots in the boundary layer can occur that results in strong upward motion in that direction.

Braun et al. (2003) show evidence of a quasi-mode in their simulation of Hurricane Bonnie (1998). In that case, the vortex tilt is only slightly to the left of the shear direction and both the relative-flow mechanism of Bender (1997) and the vortex tilt are consistent with the wavenumber 1 asymmetry in vertical motion. They argue that both mechanisms should give approximately the same answer since each is fundamentally dependent on the characteristics of the shear. In the simulation of Erin, even with the tilt and shear directions being approximately at right angles to each other, both mechanisms are qualitatively consistent with the implied vertical motion asymmetry. The relative-flow mechanism is qualitatively in agreement with the asymmetry except that, at upper levels (Fig. 16a, 16c), the maximum divergences lies somewhat to the left of the relative outflow. In contrast, both the low-level convergence and upper-level divergence maxima are located almost exactly in the downtilt direction, although the maximum convergence at upper levels lies somewhat to the left of the tilt direction. The Erin simulation lends further support to the dynamical framework described by Reasor et al. (2003) in which the interaction of a vortex with shear is governed by the adiabatic dynamics and enhanced by moist processes.

5. Summary

In order to investigate the physical processes related to hurricane intensity change, the PSU-NCAR mesoscale model MM5 is used to simulate the development and evolution of Hurricane Erin (2001) from 0000 UTC 7 September to 0000 UTC 11 September. With three two-way interactive domains with a minimum grid spacing of 4 km, the model successfully reproduces the evolution of Erin by capturing its three phases of development: formation, intensification and maintenance. Erin develops in a weakly sheared environment on 7 September. When it crosses a warm pool of 302 K waters at 36 h (1200 UTC 8 September), it deepens

rapidly. It reaches its peak intensity by the end of 9 September and then maintains a steady intensity through 10 September. Two factors appear to contribute to the cessation of intensification: movement over cooler SST's and increasing vertical wind shear associated with an approaching upper-level low pressure system.

Comparisons of observed and simulated tracks, intensities, and wind and precipitation patterns are remarkably good. Of particular interest in this study is the model's ability to capture a transition in storm's intensity and structure between 9 and 10 September during which time the hurricane's intensification suddenly ends and its outer precipitation bands shift approximately from the northeastern to the western side of the storm. The simulation also shows indications of the initial development of a secondary eyewall. Deficiencies in the simulation are apparent in the vertical distribution of precipitation as the model tends to produce rainbands that are shallower than observed. However, despite this discrepancy, the simulated vertical structure of the temperature anomaly field is in very good agreement with observations in terms of the magnitude and height of the warm core.

The simulation is used to examine the evolution of Erin from a weak depression to an intense hurricane and to describe the structural changes that occur. Erin's formation stage is characterized by highly asymmetric convection that gradually intensifies the mean vortex and reduces the radius of maximum wind. Inflow during this stage is deep while outflow is confined to upper levels. During the intensification stage, characterized by a more rapid rate of deepening, the eyewall convection becomes stronger and deeper and inflow is confined to low levels while stronger outflow occurs at middle and upper levels. Strengthening wind shear during this period leads to an asymmetric distribution of precipitation with the heaviest eyewall precipitation and a wide area of the outer precipitation concentrated on the downshear-left side and more cellular

outer band convection located on the downshear-right side. The shear reaches its peak intensity near 0000 UTC 10 September, at which time intensification stops. It then maintains a nearly steady intensity as the shear gradually weakens and the precipitation pattern shifts to the western side of the storm.

Two explanations for the change in precipitation structure are examined, both related to the interaction of the storm with the large-scale wind shear. The first is related to the effects of the storm-relative flow caused by the shear (Bender 1997). In the Erin simulation, low-level convergence (divergence) occurs where there is relative inflow (outflow) in the eyewall, qualitatively consistent with this mechanism. At upper levels, a similar pattern is seen except that the maximum upper-level divergence occurs somewhat to the left of the main outflow region.

A second explanation is based upon the vortex Rossby wave framework described by Reasor et al. (2003). In this framework, upward motion is assumed to occur in the downtilt direction and the tilt behavior is governed by two types of vortex Rossby waves: a discrete, or quasi-mode and sheared vortex Rossby waves. The quasi-mode produces precession of the upper vortex relative to the lower vortex, and in the presence of weak damping, leads to a steady tilt to the left of the shear vector. In the simulation, on both 9 and 10 September, the upward motion implied by the divergence field occurs in the downtilt direction. The tilt direction rotates cyclonically approximately 45° (about 30° more than the shear vector) from 9 to 10 September. This result suggests that the primary mechanism accounting for the shift in the precipitation pattern is a change in the tilt direction caused partially by a smaller change in the shear direction as well as by a weakening of the shear that may allow the tilt direction to change relative to the shear direction.

The changes in shear are generally related to the location of the storm relative to large-scale features of the environment. Both the intensity and direction of the shear, as well as the associated relative flow, change as the hurricane moves relative to an approaching upper trough and to surrounding high pressure systems. This result suggests that some degree of predictability of a storm's intensity and precipitation structure should exist if the evolution of the large-scale flow and the track of the storm can be reasonably predicted.

Acknowledgments. The authors gratefully acknowledge Dr. Michael Montgomery for many helpful discussions on this work and Dr. Mark Powell for providing the surface wind analyses. This work was supported by Dr. Ramesh Kakar at NASA Headquarters with funds from the NASA CAMEX-4 program.

References

- Bender, M. A., 1997: The effect of relative flow on the asymmetric structure in the interior of hurricanes. *J. Atmos. Sci.*, **54**, 703-724.
- Black, M. L., R. W. Burpee, and F. D. Marks, Jr., 1996: Vertical motion characteristics of tropical cyclones determined with airborne Doppler radial velocities. *J. Atmos. Sci.*, **53**, 1887-1909.
- , J. F. Gamache, F. D. Marks Jr., C. E. Samsury, and H. E. Willoughby, 2002: Eastern Pacific Hurricanes Jimena of 1991 and Olivia of 1994: The effect of vertical shear on structure and intensity. *Mon. Wea. Rev.*, **130**, 2291-2311.
- Black, P. G., and F. D. Marks, Jr., 1991: The structure of an eyewall mesovortex in Hurricane Hugo (1989). Preprints, *19th Conf. on Hurricanes and Tropical Meteorology*, Miami, FL, Amer. Meteor. Soc., 579-582.
- Bosart, L. E., C. S. Velden, W. E. Bracken, J. Molinari, and P. G. Black, 2000: Environmental influences on the rapid intensification of Hurricane Opal (1995) over the Gulf of Mexico. *Mon. Wea. Rev.*, **128**, 322-352.
- Braun, S. A., 2002: A cloud-resolving simulation of Hurricane Bob (1991): Storm structure and eyewall buoyancy. *Mon. Wea. Rev.*, **130**, 1573-1591.
- , and W.-K. Tao, 2000: Sensitivity of high-resolution simulation of Hurricane Bob (1991) to planetary boundary layer parameterizations. *Mon. Wea. Rev.*, **128**, 3941-3961.
- , M. T. Montgomery, and Z. Pu, 2003: The Organization of vertical motion in an asymmetric Hurricane – Bonnie (1998). Submitted to *J. Atmos. Sci.*
- Chan, J.-C. L., Y. Duan, and L. K. Shay, 2001: Tropical cyclone intensity change from a simple ocean-atmosphere coupled model. *J. Atmos. Sci.*, **58**, 154-172.

- Chen, Y., and M. K. Yau, 2001: Spiral bands in a simulated hurricane. Part I: Vortex Rossby wave verification. *J. Atmos. Sci.*, **58**, 2128-2145.
- Corbosiero, K. L., and J. Molinari, 2003: The Relationship between Storm Motion, Vertical Wind Shear, and Convective Asymmetries in Tropical Cyclones, *J. Atmos. Sci.*, **60**, 366-376.
- Dudhia, J., 1989: Numerical study of convection observed during the winter monsoon experiment using a mesoscale two-dimensional model. *J. Atmos. Sci.*, **46**, 3077-3107.
- , 1993: A nonhydrostatic version of the Penn State-NCAR mesoscale model: Validation tests and simulation of an Atlantic Cyclone and cold front. *Mon. Wea. Rev.*, **121**, 1493-1513.
- Davis, C. A., and L. F. Bosart, 2001: Numerical simulations of the genesis of Hurricane Diana (1984). Part I: Control simulation. *Mon. Wea. Rev.*, **129**, 1859-1881.
- , and ———, 2002: Numerical simulations of the genesis of Hurricane Diana (1984). Part II: Sensitivity of track and intensity prediction. *Mon. Wea. Rev.*, **130**, 1100-1124.
- Emanuel, K. A., 1988: The maximum intensity of hurricanes. *J. Atmos. Sci.*, **45**, 1143-1155.
- , 1989: The finite-amplitude nature of tropical cyclogenesis. *J. Atmos. Sci.*, **46**, 3431-3456.
- Flatau, M., W. H. Schubert, and D. E. Stevens, 1994: The role of baroclinic processes in tropical cyclone motion: The influence of vertical tilt. *J. Atmos. Sci.*, **51**, 2589-2601.
- Frank, W. M., and E. A. Ritchie, 1999: Effects on environmental flow upon tropical cyclone structure. *Mon. Wea. Rev.*, **127**, 2044-2061.
- Frank, W. M., and E. A. Ritchie: Effects of vertical wind shear on the intensity and structure of numerically simulated hurricanes. *Mon. Wea. Rev.*, **129**, 2249-2269.
- Garratt, J. R., 1992: *The Atmospheric Boundary Layer*, Cambridge University Press, 316 pp.
- Gray, W. M., 1998: The formation of tropical cyclones. *Meteorol. Atmos. Phys.*, **67**, 37-69.

- Grell, G. A., J. Dudhia, and D. R. Stauffer, 1995: A description of the fifth-generation Penn State/NCAR Mesoscale Model (MM5). NCAR Technical Note (NCAR/TN-398+STR), 122 pp.
- Halverson, J. B., J. Simpson, G. Heymsfield, H. Pierce, T. Hock, and L. Ritchie, 2003: Warm core structure of Hurricane Erin diagnosed from high-altitude dropsondes during CAMEX-4. *J. Atmos. Sci.*, (submitted).
- Heymsfield, G. M., J. B. Halverson, and I. J. Caylor, 1999: A wintertime Gulf Coast squall line observed by EDOP airborne Doppler radar. *Mon. Wea. Rev.*, **127**, 2928-2949.
- , ———, J. Simpson, L. Tian, and T. P. Bui, 2001: ER-2 Doppler radar (EDOP) investigations of the eyewall of Hurricane Bonnie during CAMEX-3. *J. Appl. Meteor.*, **40**, 1310-1330.
- , S. W. Bidwell, P. E. Racette, I. J. Caylor, S. Ameen, S. Nicholson, W. Boncyk, L. Miller, D. Vandenmark, and L. R. Dod, 1996: The EDOP radar system on the high-altitude NASA ER-2 aircraft. *J. Atmos. Oceanic Technol.*, **13**, 795-809.
- Holland, G. J., 1997: Maximum potential intensity of tropical cyclones. *J. Atmos. Sci.*, **54**, 2519-2541.
- Jones, S. C., 1995: The evolution of vortices in vertical shear: Initially barotropic vortices. *Quart. J. Roy. Meteor. Soc.*, **121**, 821-851.
- Jorgensen, D. P., E. J. Zipser, and M. A. LeMone, 1985: Vertical motions in intense hurricanes. *J. Atmos. Sci.*, **42**, 839-856.
- Kossin, J. P. and W. H. Schubert, 2001: Mesovortices, polygonal flow patterns, and rapid pressure falls in hurricane-like vortices. *J. Atmos. Sci.*, **58**, 2196-2209.

- Lee, C.-S., 1989: Observational analysis of tropical cyclogenesis in the western North Pacific: I: Structural evolution of cloud clusters. *J. Atmos. Sci.*, **46**, 2580-2598.
- Liu, Y., D.-L. Zhang, and M. K. Yau, 1997: A multiscale numerical study of Hurricane Andrew (1992). Part I: Explicit simulation and verification. *Mon. Wea. Rev.*, **125**, 3073-3093.
- , ———, ———, 1999: A multiscale numerical study of Hurricane Andrew (1992). Part II: Kinematics and inner-core structures. *Mon. Wea. Rev.*, **127**, 2597-2616.
- Marks, F. D., and P. G. Black, 1990: Close encounter with an intense mesoscale vortex within Hurricane Hugo (September 15, 1989). *Fourth Conf. on Mesoscale Processes*, Boulder, CO, Amer. Meteor. Soc., 114-115.
- , and R. A. Houze, Jr., 1987: Inner core structure of Hurricane Alicia from airborne doppler radar observations. *J. Atmos. Sci.*, **44**, 1296-1317.
- Molinari, J., and D. Vollaro, 1989: External influences on hurricane intensity. Part I: Outflow layer eddy angular momentum fluxes. *J. Atmos. Sci.*, **46**, 1093-1105.
- , and ———, 1990: External influences on hurricane intensity. Part II: Vertical structure and response of the hurricane vortex. *J. Atmos. Sci.*, **47**, 1902-1918.
- , S. Skubis, and D. Vollaro, 1995: External influences on hurricane intensity. Part III: Potential vorticity structure. *J. Atmos. Sci.*, **52**, 3593-3606.
- , ———, ———, F. Alsheimer, and H. E. Willoughby, 1998: Potential vorticity analysis of tropical cyclone intensification. *J. Atmos. Sci.*, **55**, 2632-2644.
- Montgomery, M. T., and J. Enagonio, 1998: Tropical cyclogenesis via convectively forced vortex Rossby waves in a three-dimensional quasigeostrophic model. *J. Atmos. Sci.*, **55**, 3176-3207.

- , and R. J. Kallenbach, 1997: A theory for vortex Rossby-waves and its application to spiral bands and intensity changes in hurricanes. *Quart. J. Roy. Meteor. Soc.*, **123**, 435-465.
- Neuman, C. J., 1997: National plan for tropical cyclone research. FCM rep. FCM-P25-1997, 100 pp. [Available from Office of the Federal Coordinator for Meteorological Services and Supporting Research, 8455 Colesville Ave., Suite 1500, Silver Spring, MD 20910.]
- Ooyama, K., 1969: Numerical simulation of the life cycle of tropical cyclones. *J. Atmos. Sci.*, **26**, 3-40.
- Pagowski, M., and G. W. K. Moore, 2001: A numerical study of an extreme cold-air outbreak over the Labrador Sea: Sea ice, air-sea interaction, and development of polar lows. *Mon. Wea. Rev.*, **129**, 2023-2039.
- Raymond, D. J., 1992: Nonlinear balance and potential-vorticity thinking at large Rossby number. *Quart. J. Roy. Meteor. Soc.*, **118**, 987-1015.
- Reasor, P. D., and M. T. Montgomery, and L. D. Grasso, 2003: A new look at the problem of tropical cyclones in vertical shear flow: Vortex resiliency. *J. Atmos. Sci.*, (submitted).
- , ———, F. D. Marks Jr., and J. F. Gamache, 2000: Low-wavenumber structure and evolution of the hurricane inner core observed by airborne dual-Doppler radar. *Mon. wea. Rev.*, **128**, 1653-1680.
- Schubert, W. H., M. T. Montgomery, R. K. Taft, T. A. Guinn, S. R. Fulton, J. P. Kossin, and J. P. Edwards, 1999: Polygonal eyewalls, asymmetric eye contraction, and potential vorticity mixing in hurricanes. *J. Atmos. Sci.*, **56**, 1197-1223.
- Shay, L. K., G. J. Goni, and P. G. Black, 2000: Role of a warm ocean feature on Hurricane Opal. *Mon. Wea. Rev.*, **128**, 1366-1388.

- Wang, B., and X. Li, 1992: The beta drift of three-dimensional vortices: A numerical study. *Mon. Wea. Rev.*, **120**, 579-593.
- Wang, Y., and G. J. Holland, 1996: The beta drift of baroclinic vortices. Part I: Adiabatic vortices. *J. Atmos. Sci.*, **53**, 411-427.
- Willoughby, H. E., F. D. Marks, Jr., and R. J. Feinberg, 1984: Stationary and moving convective bands in hurricanes. *J. Atmos. Sci.*, **41**, 3189-3211.
- Zehr, R. M., 2002: Vertical wind shear characteristics with Atlantic hurricanes during 2001. Preprints, *25th Conf. on Hurricanes and Tropical Meteorology*, San Diego, California, Amer. Meteor. Soc., 170-171.
- Zhu, T., D.-L. Zhang, and F. Weng, 2003: Numerical simulation of hurricane Bonnie (1998). Part I: Eyewall evolution and intensity changes. *Mon. Wea. Rev.*, (submitted).

Figure Captions

Figure 1. Initial fields for (a) winds at 1000 mb and surface pressure at intervals of 1 mb and (b) sea-surface temperature (K) from the NECP analysis at intervals of 1 K. The simulated track of Erin is also presented in (b) and the numbers represent the integration hours.

Figure 2. (a) The maximum wind at the lowest model level and (b) minimum central pressure of Hurricane Erin from best track data (solid) and the simulation (dotted).

Figure 3. The observed (solid dots) and simulated tracks (open squares) from 0000 UTC 7 September to 0000 UTC 11. The numbers for the observed track show the corresponding integration hours. Open squares are plotted every 12 h (see also Fig. 1b).

Figure 4. Comparison of (a) the observed surface wind analysis at 1930Z (courtesy of Mark Powell) with (b) the model simulated wind at the lowest level at 2000 UTC 9 September, 2001. The contour interval is 3 m s^{-1} in both panels.

Figure 5. Same as Fig. 4, but for an observed surface analysis at 1819 UTC and a simulated wind field at 1800 UTC on Sept. 10, 2001.

Figure 6. TRMM rainfall rate (left panels) at 1011 UTC (top), 1326 UTC (middle) and 1504 UTC (bottom) and the simulated reflectivity (right panels) at 1000 UTC (top), 1300 UTC

(middle) and 1500 UTC (bottom) on Sept. 9, 2001. The domain is 300 by 300 km. The arrows indicate the shear direction between 1-10 km.

Figure 7. Same as Fig. 6, but for the TRMM rainfall rate (left panels) at 1142 UTC (top), 1315 UTC (middle) and 1447 UTC (bottom) and the simulated reflectivity (right panels) at 1200 UTC (top), 1300 UTC (middle) and 1500 UTC (bottom) on Sept. 10, 2001.

Figure 8. Vertical cross sections of radar reflectivity and estimated vertical air motion from EDOP for flight legs (a, b) along a northwest to southeast pass from approximately 1754-1836 UTC and (c, d) along a west to east pass from 1906 to 1950 UTC 10 September 2001.

Figure 9. Vertical cross sections of vertical motion (contours) and simulated radar reflectivity (shading) through Erin's core at (a) 1800 and (b) 1900 UTC 10 September along the two lines shown in (c), in which the simulated radar reflectivity at 1900 UTC is also shown. The intervals for vertical motion are 0.5 m s^{-1} for negative values (dashed lines) and 1 m s^{-1} for positive values (solid lines). The zero contour is excluded.

Figure 10. (a) Cross section of observed temperature anomaly through Erin's core on 10 September [adapted from Halverson et al. (2003)] and (b) the simulated temperature anomaly and radar reflectivity at 1700 UTC 10 September.

Figure 11. Time-radius distribution of the symmetric components of the simulated radar reflectivity (shading) and total wind speed (contours) at the lowest model level (38 m). The contour interval for wind speed is 5 m s^{-1} .

Figure 12. (a) Time series of the azimuthally and radially averaged distributions of radial and vertical velocities. The radial wind (contours) is averaged over 48-100 km radius while vertical motion (shaded) is averaged over 28-80 km radius. (b) Time series of the area-averaged ground-relative horizontal winds averaged over a circle of 300 km radius.

Figure 13. Vertical cross section of tangential wind (contours, at intervals of 5 m s^{-1}) and mean secondary circulation (vectors) at 0000 UTC 11 September (96 h).

Figure 14. Vector winds and geopotential height fields at 200 mb in (a, c, e) and 850 mb in (b, d, f) for (a, b) 1200 UTC 8 September, (c, d) 1200 UTC 9 September, and (e, f) 1200 UTC 10 September. Geopotential height contours are drawn at intervals of 20 m. The center of Erin at each time is indicated with closed dots. The vector scale is shown below center.

Figure 15. Twenty-four hour mean simulated radar reflectivity and asymmetric winds averaged over (a) 9 September and (b) 10 September at 38 m. The asymmetric wind vectors are calculated based on the surface center location. The thick arrows denote the directions of shear vectors for each day.

Figure 16. Mean divergence and asymmetric winds averaged over (a) 9 September at 7500 m, (b) 9 September at 38 m, (c) 10 September at 7500 m (d) 10 September at 38 m. The asymmetric wind vectors are calculated based on the center locations at the respective heights. The thick arrows denote the directions of shear vectors (solid) and tilt vectors (open).

Figure 17. Hovmoller diagram of radially averaged (16-100 km) vertical motion (contours, 0.2 m s⁻¹ intervals) and potential temperature (shading; dark gray, 326 K; medium gray, 327 K; light gray, 328 K). The thick solid curve indicates the direction of vortex tilt as indicated by the location of the 8-km center relative to the surface center.

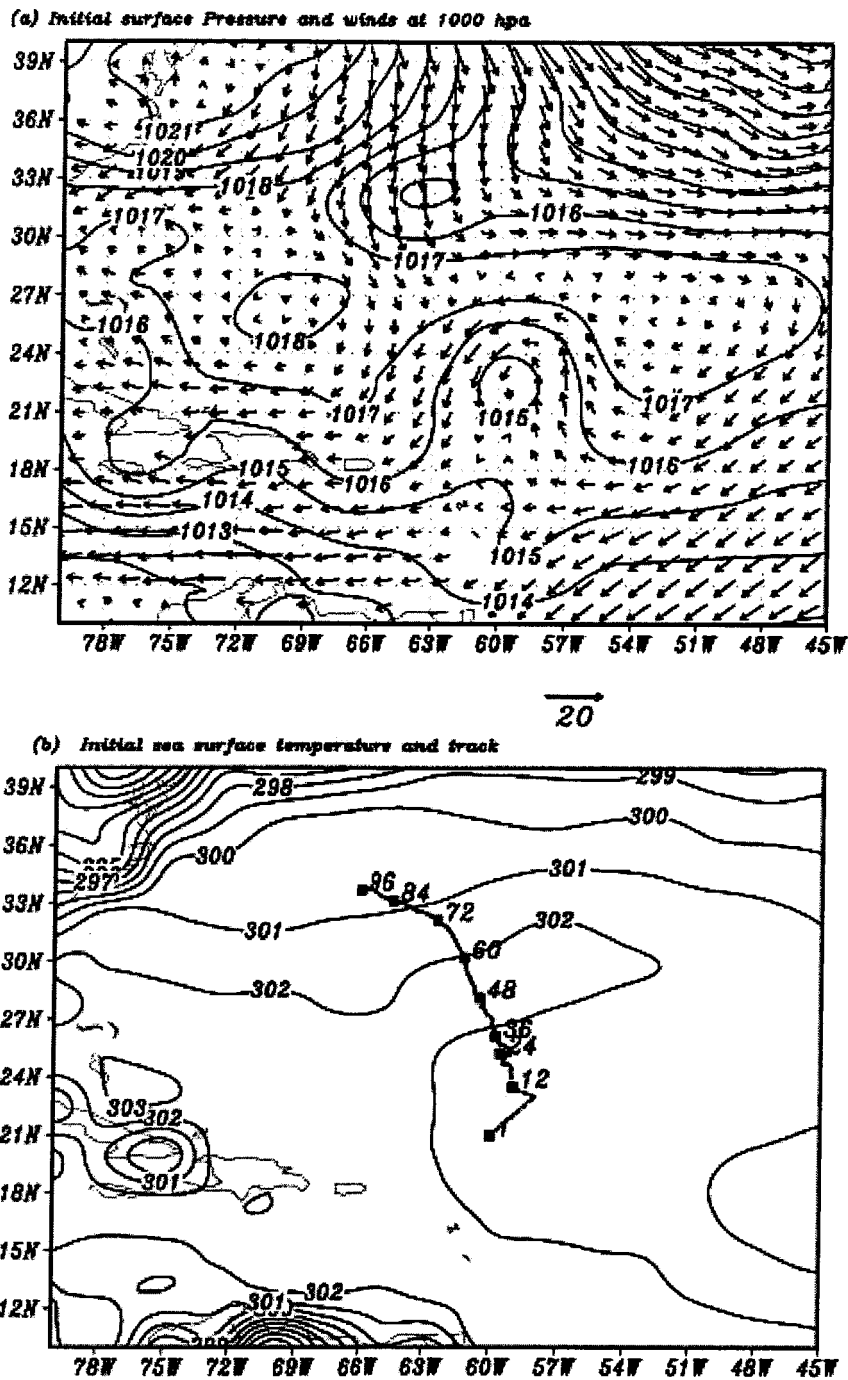


Figure 1. Initial fields for (a) winds at 1000 mb and surface pressure at intervals of 1 mb and (b) sea-surface temperature (K) from the NECP analysis at intervals of 1 K. The simulated track of Erin is also presented in (b) and the numbers represent the integration hours.

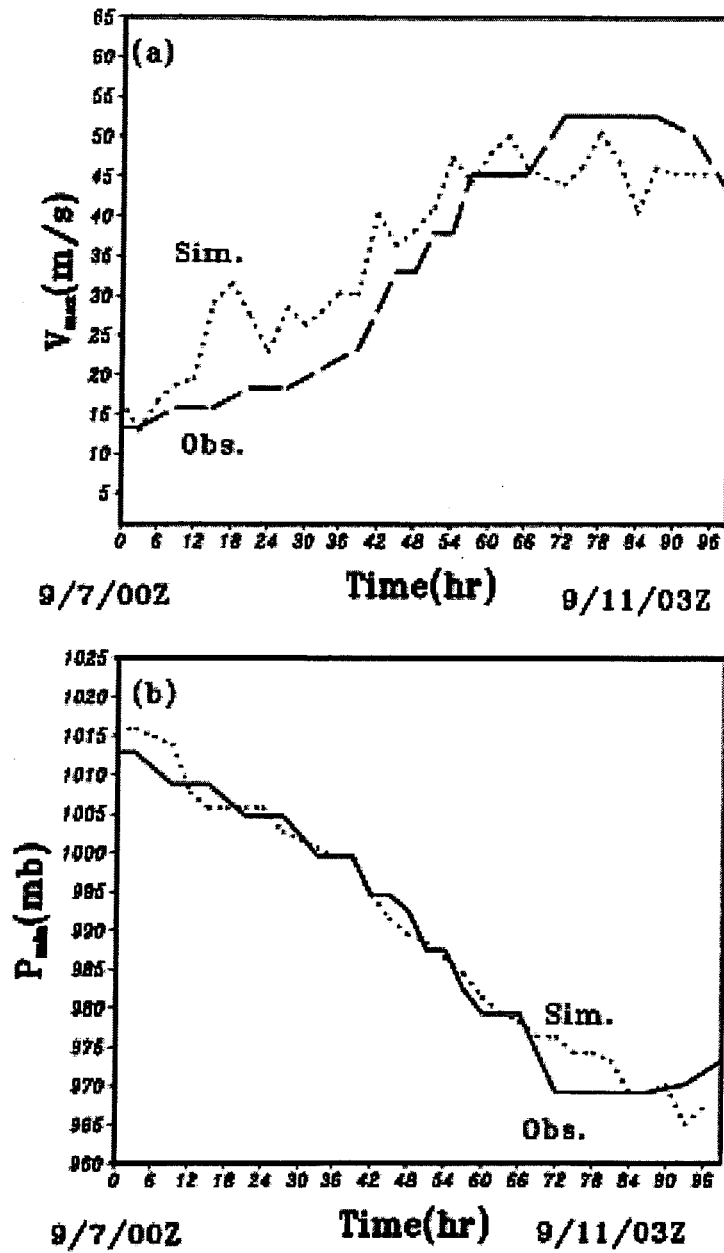


Figure 2. (a) The maximum wind at the lowest model level and (b) minimum central pressure of Hurricane Erin from best track data (solid) and the simulation (dotted).

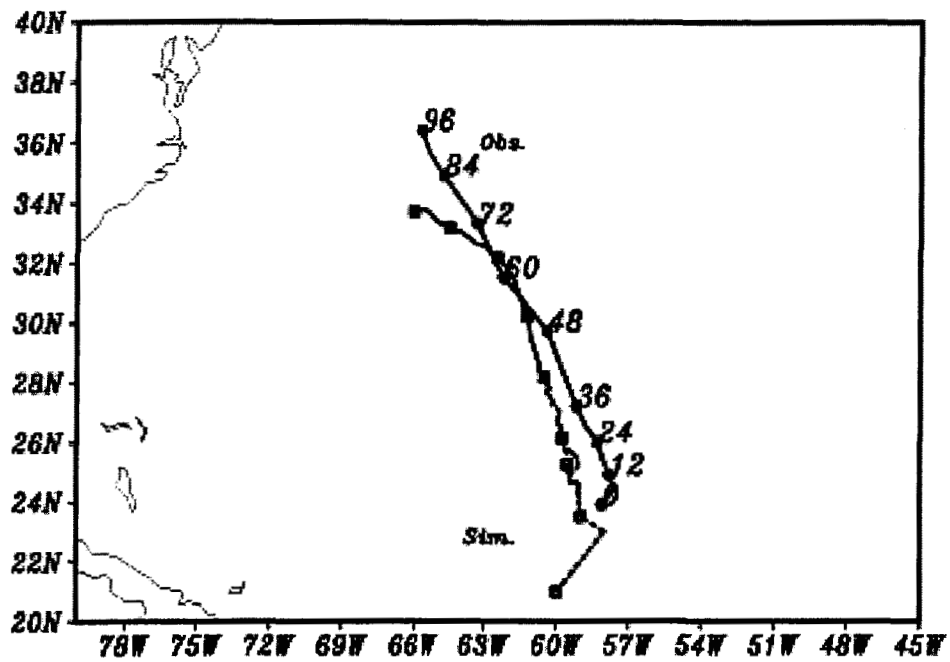


Figure 3. The observed (solid dots) and simulated tracks (open squares) from 0000 UTC 7 September to 0000 UTC 11. The numbers for the observed track show the corresponding integration hours. Open squares are plotted every 12 h (see also Fig. 1b).

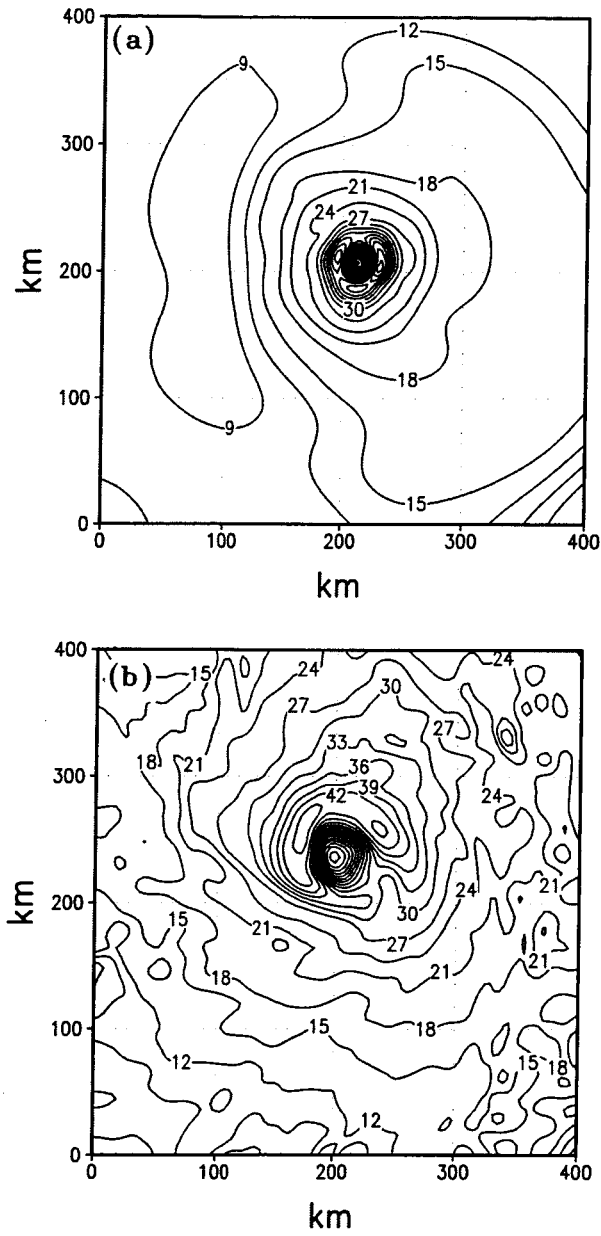


Figure 4. Comparison of (a) the observed surface wind analysis at 1930Z (courtesy of Mark Powell) with (b) the model simulated wind at the lowest level at 2000 UTC 9 September, 2001. The contour interval is 3 m s^{-1} in both panels.

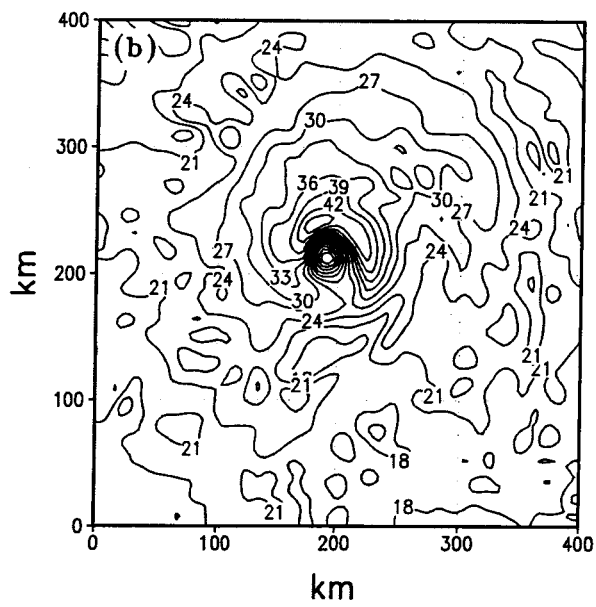
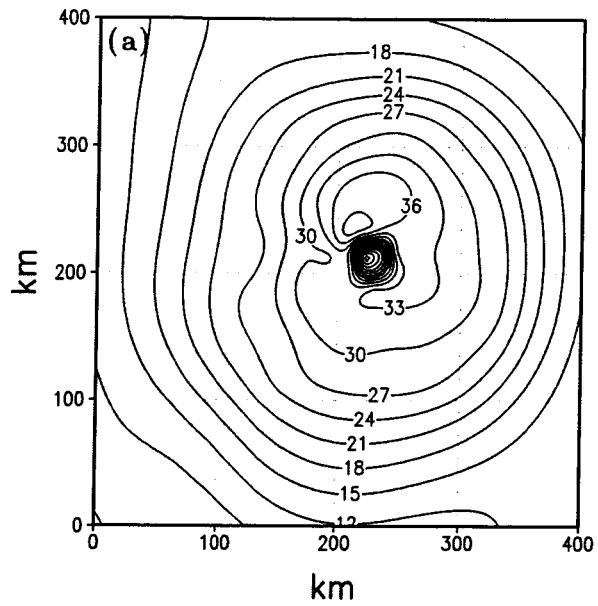


Figure 5. Same as Fig. 4, but for an observed surface analysis at 1819 UTC and a simulated wind field at 1800 UTC on Sept. 10, 2001.

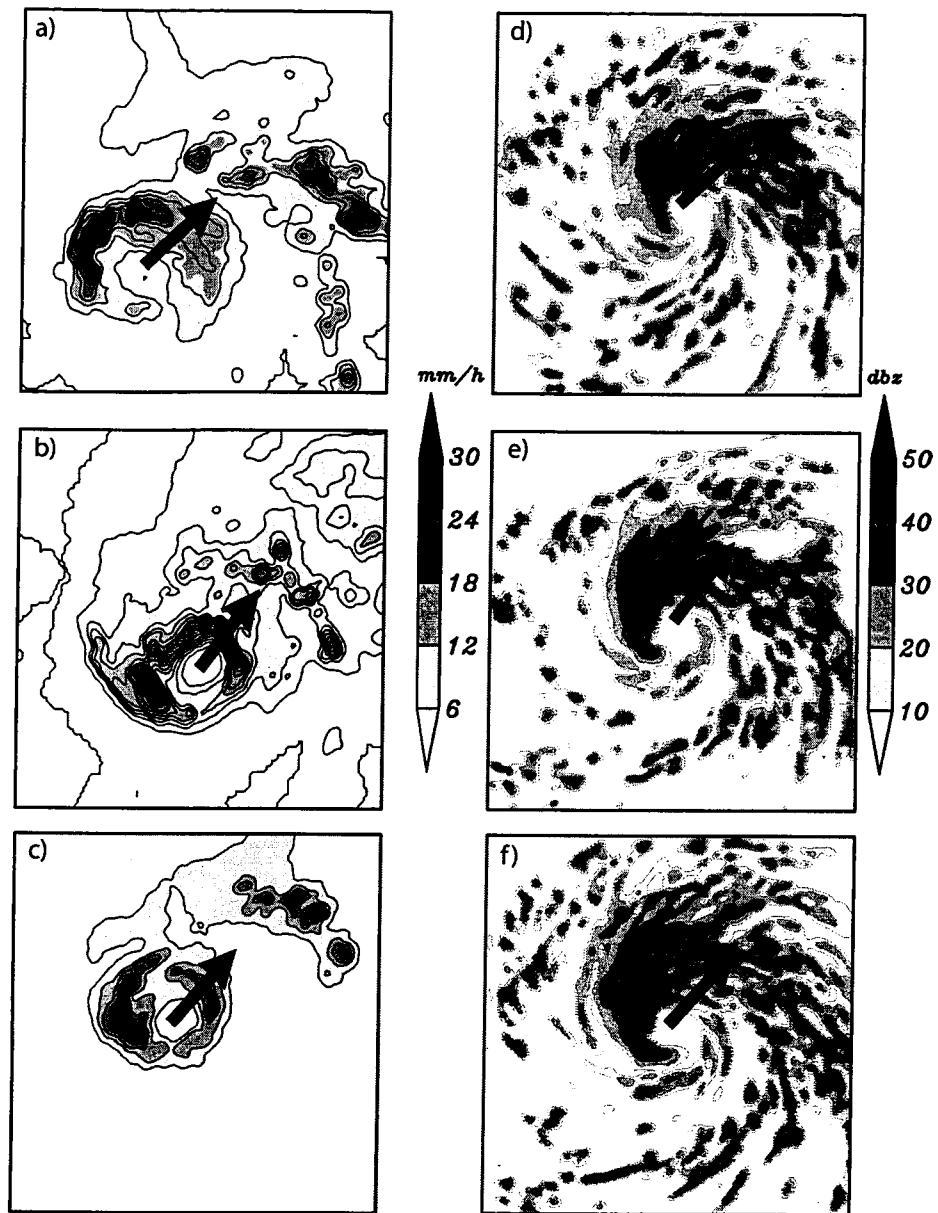


Figure 6. TRMM rainfall rate (left panels) at 1011 UTC (top), 1326 UTC (middle) and 1504 UTC (bottom) and the simulated reflectivity (right panels) at 1000 UTC (top), 1300 UTC (middle) and 1500 UTC (bottom) on Sept. 9, 2001. The domain is 300 by 300 km. The arrows indicate the shear direction between 1-10 km.

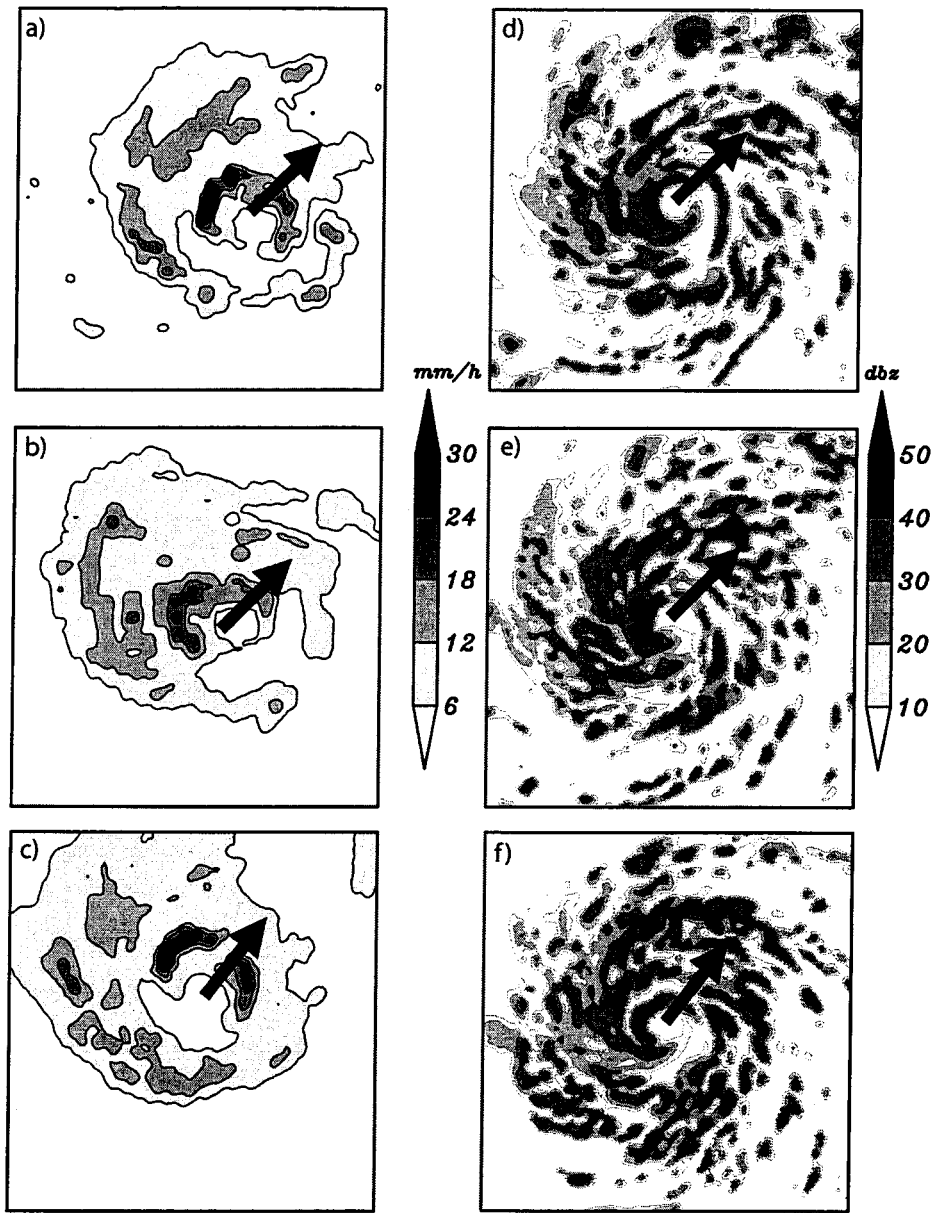


Figure 7. Same as Fig. 6, but for the TRMM rainfall rate (left panels) at 1142 UTC (top), 1315 UTC (middle) and 1447 UTC (bottom) and the simulated reflectivity (right panels) at 1200 UTC (top), 1300 UTC (middle) and 1500 UTC (bottom) on Sept. 10, 2001.

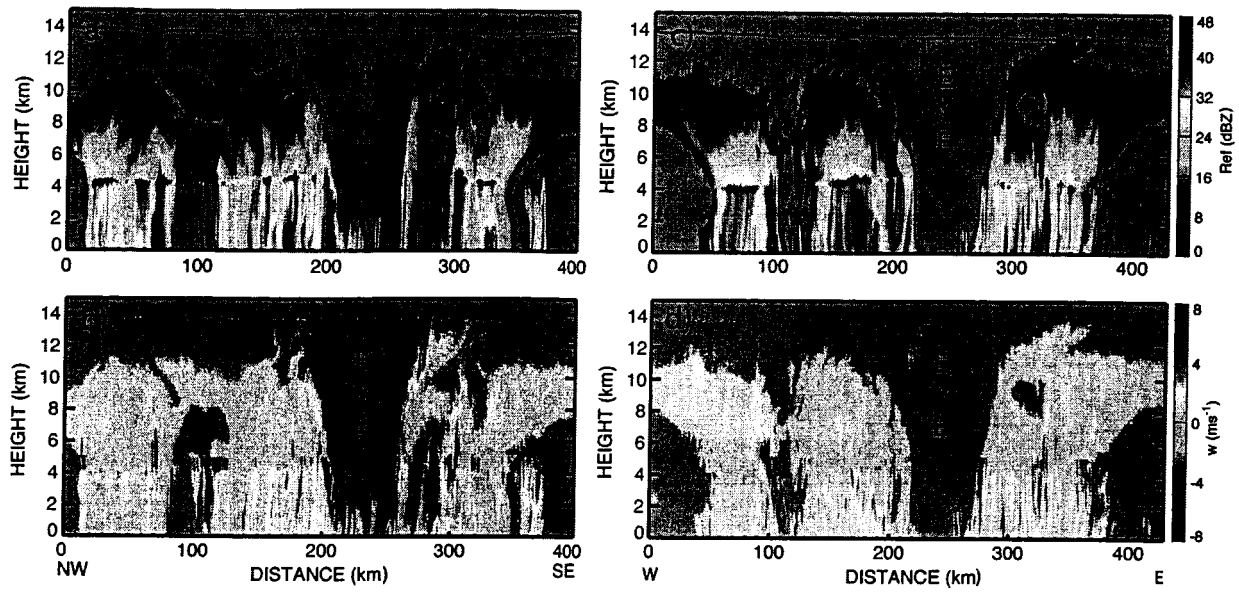


Figure 8. Vertical cross sections of radar reflectivity and estimated vertical air motion from EDOP for flight legs (a, b) along a northwest to southeast pass from approximately 1754-1836 UTC and (c, d) along a west to east pass from 1906 to 1950 UTC 10 September 2001.

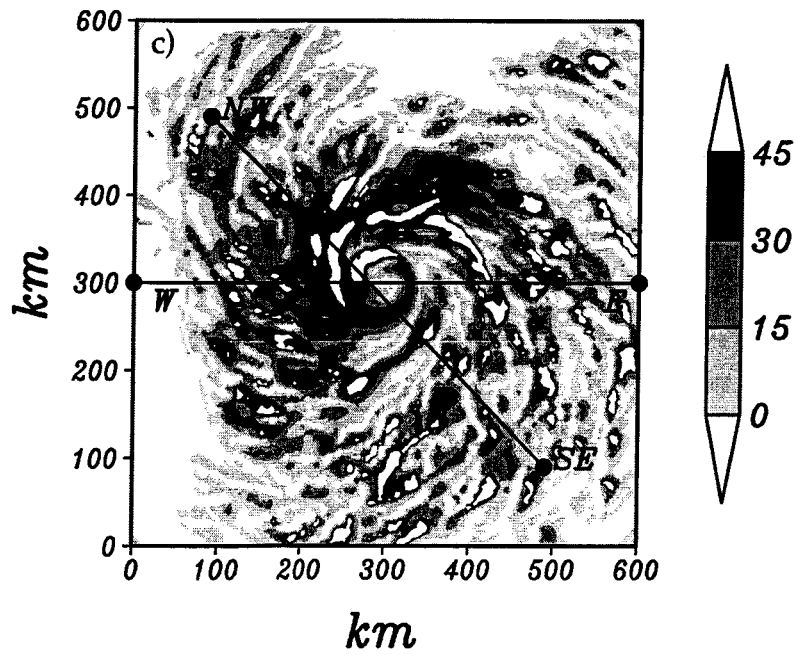
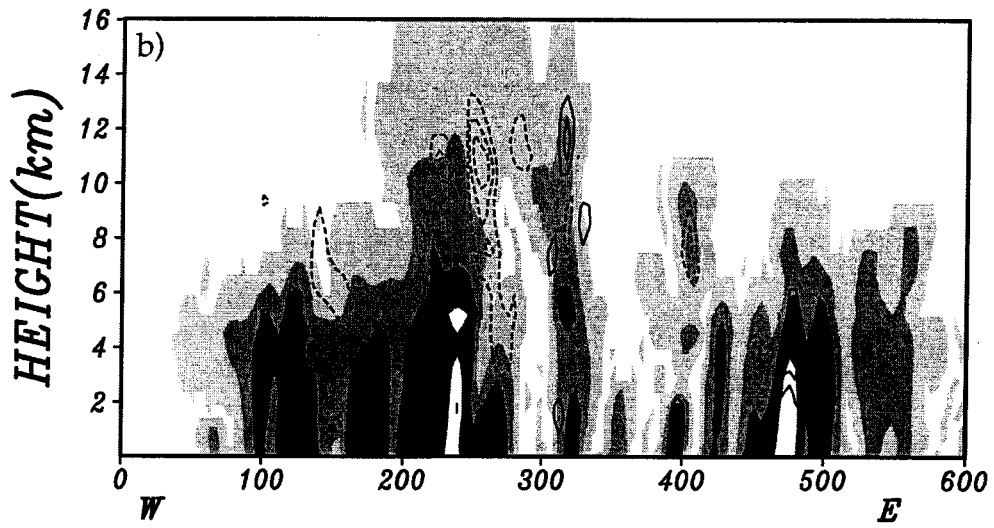
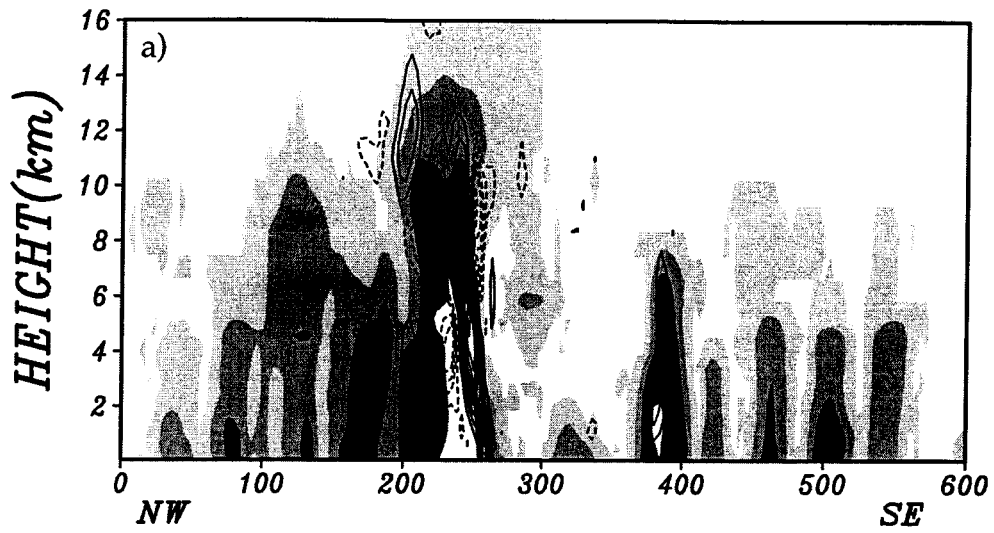


Figure 9. Vertical cross sections of vertical motion (contours) and simulated radar reflectivity (shading) through Erin's core at (a) 1800 and (b) 1900 UTC 10 September along the two lines shown in (c), in which the simulated radar reflectivity at 1900 UTC is also shown. The intervals for vertical motion are 0.5 m s^{-1} for negative values (dashed lines) and 1 m s^{-1} for positive values (solid lines). The zero contour is excluded.

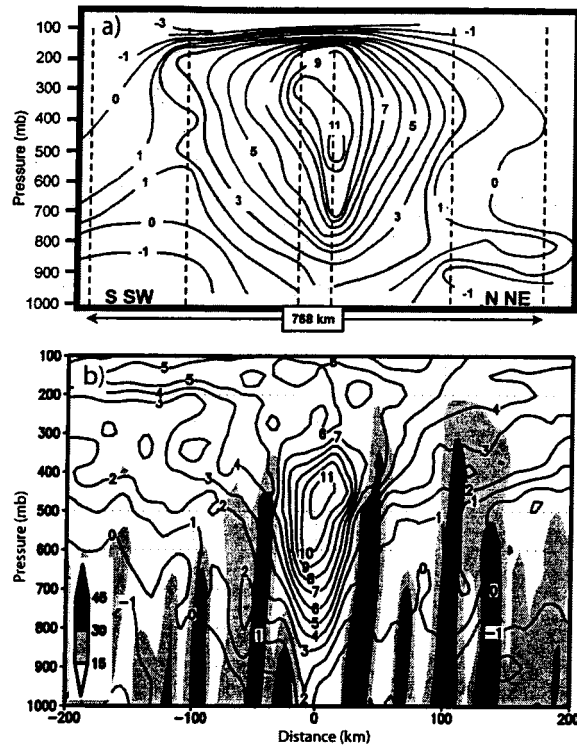


Figure 10. (a) Cross section of observed temperature anomaly through Erin's core on 10 September [adapted from Halverson et al. (2003)] and (b) the simulated temperature anomaly and radar reflectivity at 1700 UTC 10 September. The contour interval for temperature is 1 K.

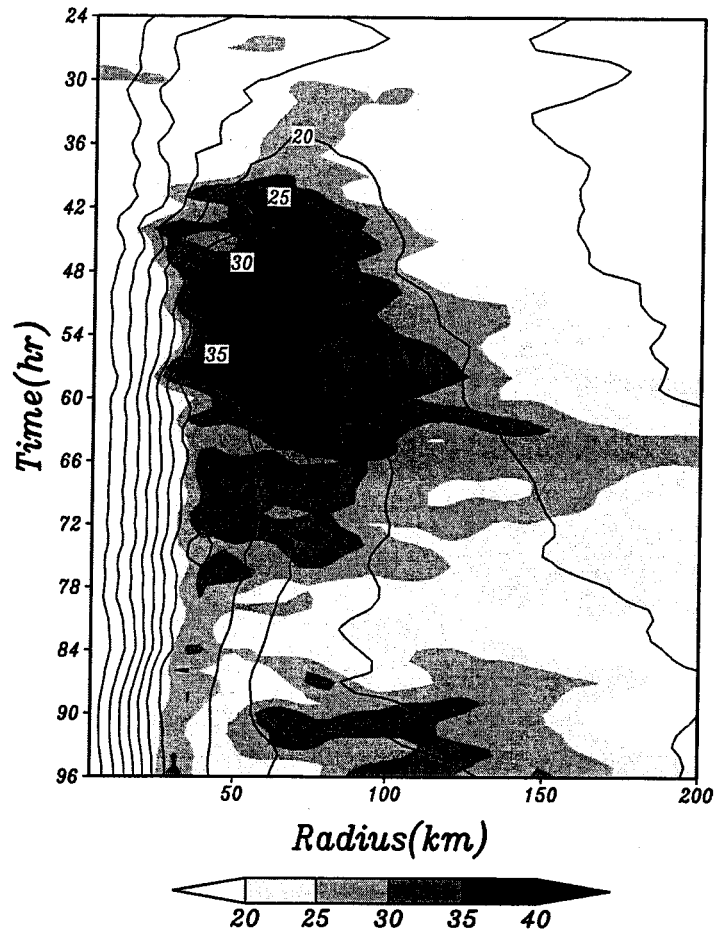


Figure 11. Time-radius distribution of the symmetric components of the simulated radar reflectivity (shading) and total wind speed (contours) at the lowest model level (38 m). The contour interval for wind speed is 5 m s^{-1} .

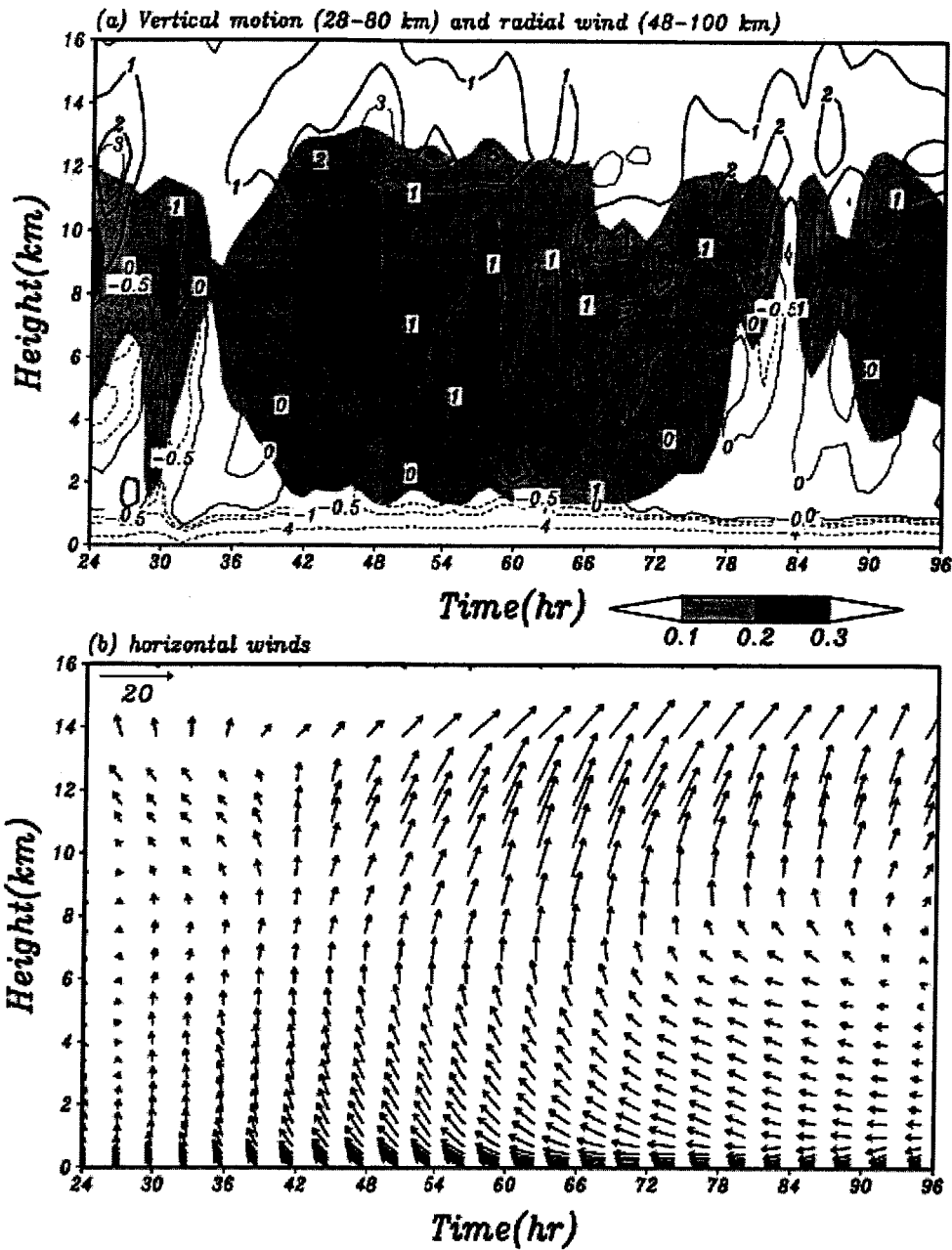


Figure 12. (a) Time series of the azimuthally and radially averaged distributions of radial and vertical velocities. The radial wind (contours) is averaged over 48-100 km radius while vertical motion (shaded) is averaged over 28-80 km radius. (b) Time series of the area-averaged ground-relative horizontal winds averaged over a circle of 300 km radius.

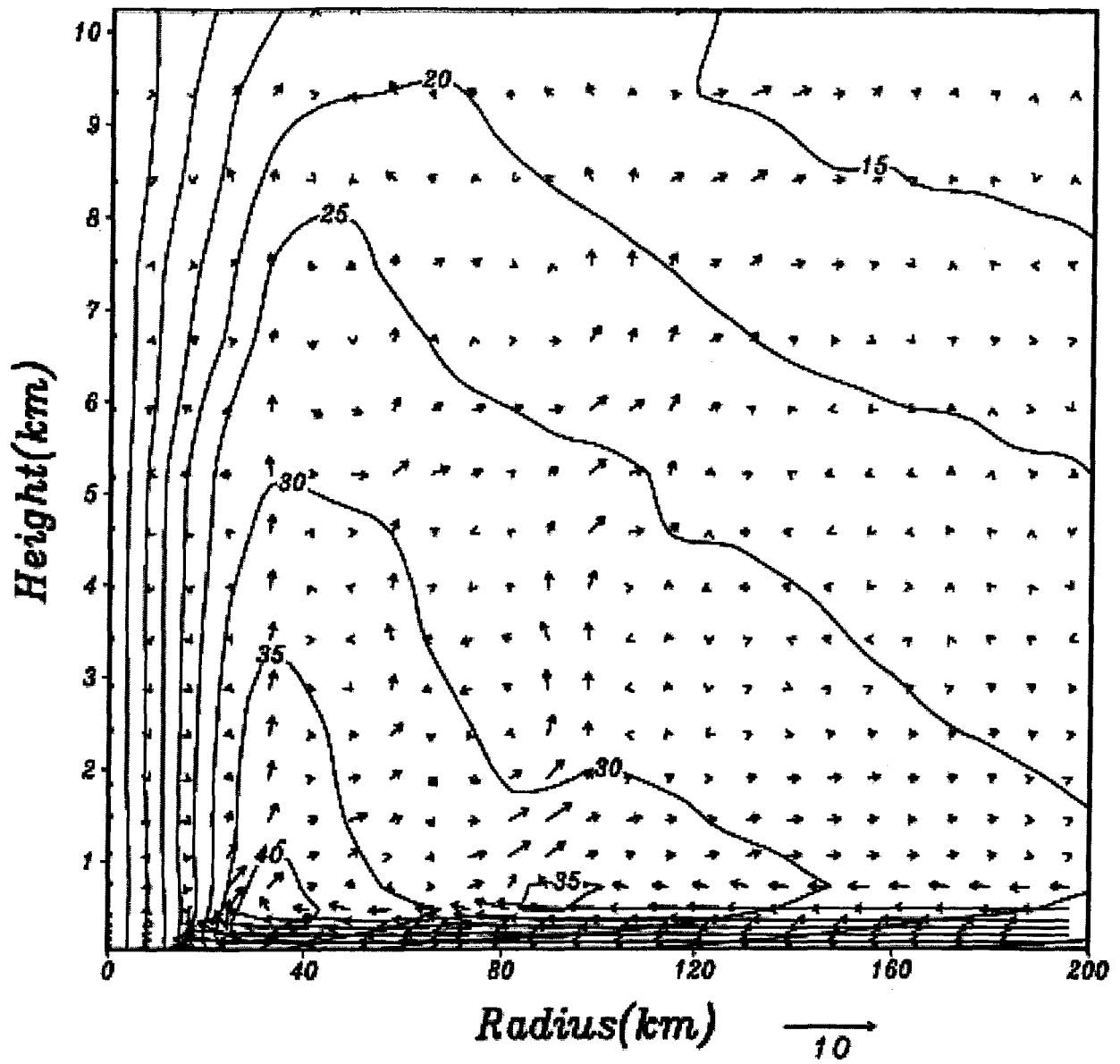


Figure 13. Vertical cross section of tangential wind (contours, at intervals of 5 m s^{-1}) and mean secondary circulation (vectors) at 0000 UTC 11 September (96 h).

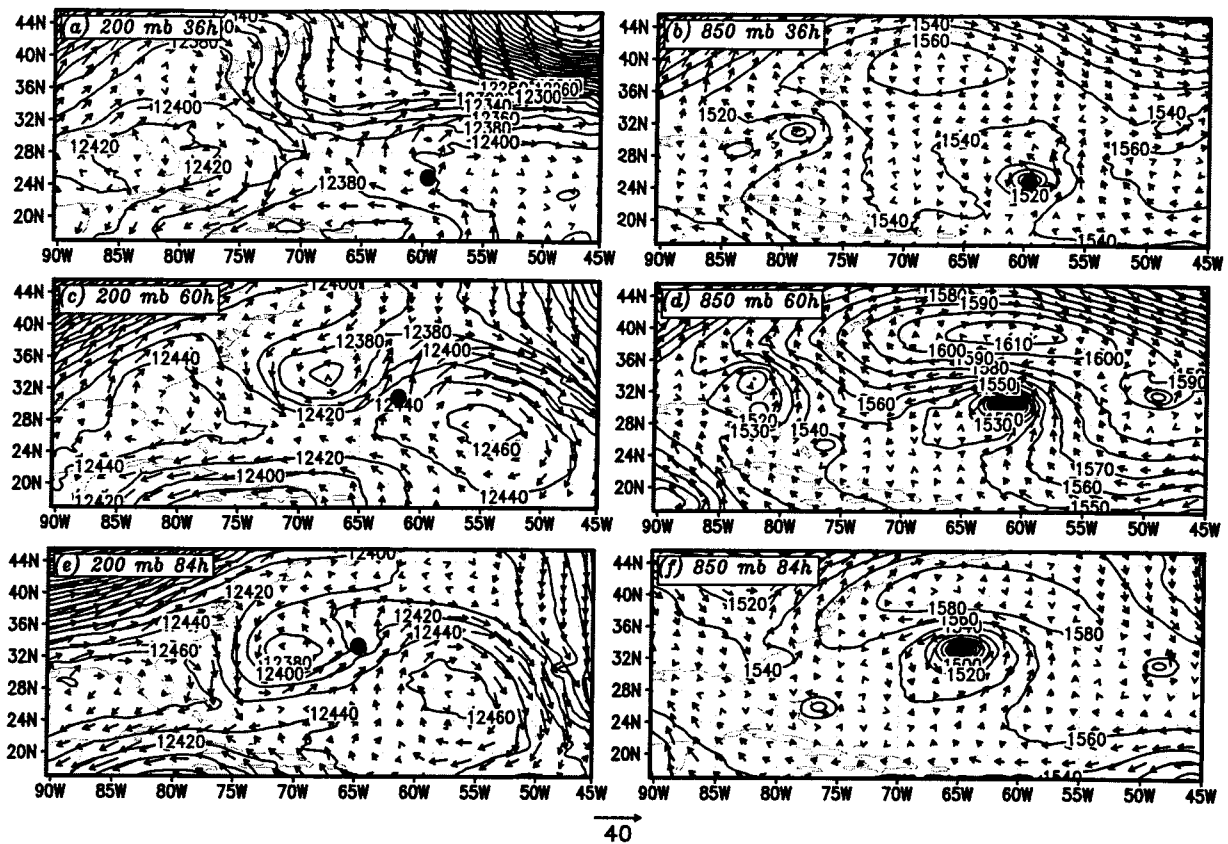


Figure 14. Vector winds and geopotential height fields at 200 mb in (a, c, e) and 850 mb in (b, d, f) for (a, b) 1200 UTC 8 September, (c, d) 1200 UTC 9 September, and (e, f) 1200 UTC 10 September. Geopotential height contours are drawn at intervals of 20 m. The center of Erin at each time is indicated with closed dots. The vector scale is shown below center.

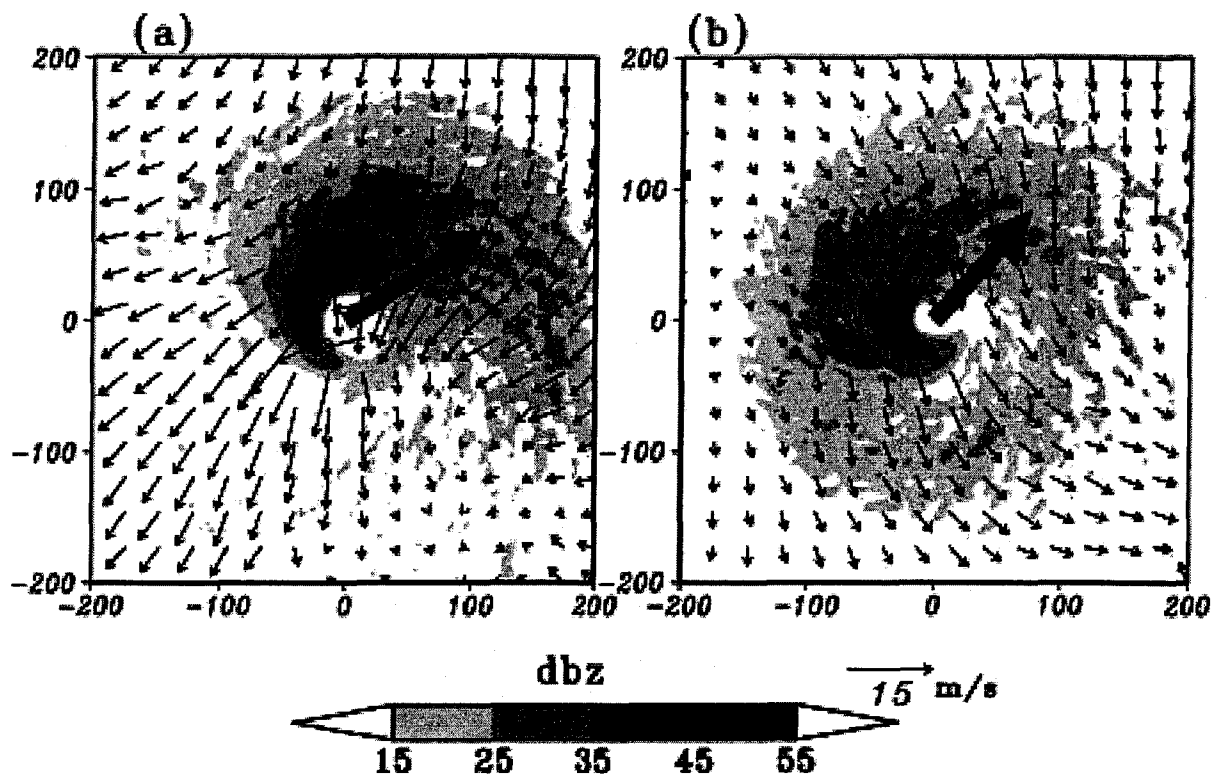


Figure 15. Twenty-four hour mean simulated radar reflectivity and asymmetric winds averaged over (a) 9 September and (b) 10 September at 38 m. The asymmetric wind vectors are calculated based on the surface center location. The thick arrows denote the directions of shear vectors for each day.

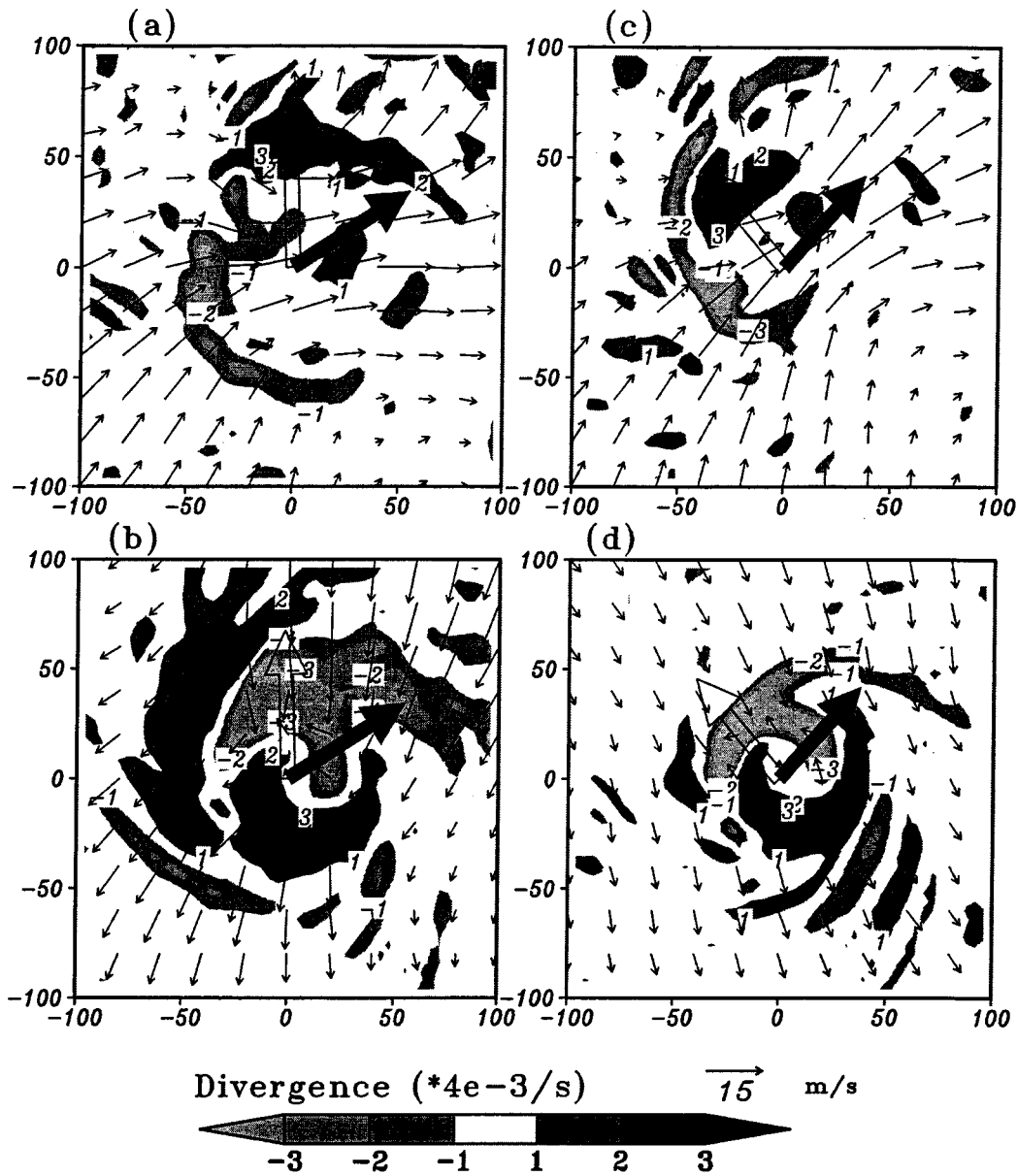


Figure 16. Mean divergence and asymmetric winds averaged over (a) 9 September at 7500 m, (b) 9 September at 38 m, (c) 10 September at 7500 m (d) 10 September at 38 m. The asymmetric wind vectors are calculated based on the center locations at the respective heights. The thick arrows denote the directions of shear vectors (solid) and tilt vectors (open).

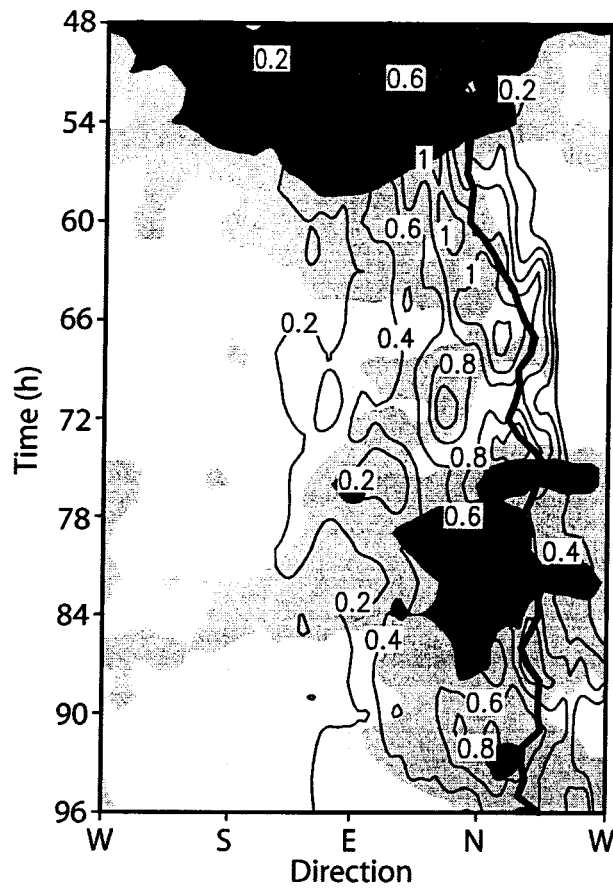


Figure 17. Hovmoller diagram of radially averaged (16-100 km) vertical motion (contours, 0.2 m s⁻¹ intervals) and potential temperature (shading; dark gray, 326 K; medium gray, 327 K; light gray, 328 K). The thick solid curve indicates the direction of vortex tilt as indicated by the location of the 8-km center relative to the surface center.